The Effects of Late Cenozoic Climate Change on the Global Distribution of Frost Cracking

Hemanti Sharma[1], Sebastian G. Mutz[1], Todd A. Ehlers[1*]

[1]Department of Geosciences, University of Tuebingen, Tuebingen, 72076, Germany

*Correspondence to: Todd A. Ehlers (todd.ehlers@uni-tuebingen.de)

Abstract. Frost cracking is a dominant mechanical weathering phenomenon facilitating the breakdown of bedrock in periglacial regions. Despite recent advances in understanding frost cracking processes, few studies have addressed how global climate change over the Late Cenozoic may have impacted spatial variations in frost cracking intensity. In this study, we estimate global changes in frost cracking intensity (FCI) by segregation ice growth. Existing process-based models of FCI are applied in combination with soil thickness data from the Harmonized World Soil Database. Temporal and spatial variations in FCI are predicted using surface temperatures changes obtained from ECHAM5 general circulation model simulations conducted for four different paleoclimate time-slices. Time-slices considered include Pre-Industrial (~1850 CE, PI), Mid-Holocene (~6 ka, MH), Last Glacial Maximum (~21 ka, LGM) and Pliocene (~3 Ma, PLIO) times. Results indicate for all paleoclimate time slices that frost cracking was most prevalent (relative to PI times) in the mid to high latitude regions, as well as high-elevation lower latitudes areas such the Himalayas, Tibet, European Alps, the Japanese Alps, the USA Rocky Mountains, and the Andes Mountains. The smallest deviations in frost cracking (relative to PI conditions) were observed in the MH simulation, which yielded slightly higher FCI values in most of the areas. In contrast, larger deviations were observed in the simulations of the colder climate (LGM) and warmer climate (PLIO). Our results indicate that the impact of climate change on frost cracking was most severe during the PI – LGM period due to higher differences in temperatures and glaciation at higher latitudes. The PLIO results indicate low FCI in the Andes and higher values of FCI in Greenland and Canada due to the diminished extent of glaciation in the warmer PLIO climate.

Keywords: Climate Change, frost cracking, physical weathering, Pre-Industrial, Mid-Holocene, Last Glacial Maximum, Pliocene

1. Introduction

Climate change, mountain building, and erosion are closely linked over different spatial and temporal scales (e.g. Whipple, 2009; Adams et al., 2020). Over million year timescales, mountain building alters global climate by introducing physical obstacles to atmospheric flow (Raymo and Ruddiman, 1992) that influences regional temperatures and precipitation (Botsyun et al., 2020; Ehlers and Poulsen, 2009; Mutz et al., 2018; Mutz and Ehlers, 2019). Over decadal to million-year time scales, climate change impacts the erosion of mountains in several ways, such as through the modification of vegetation cover (e.g. Acosta et al., 2015; Schmid et al., 2018; Werner et al., 2018; Starke et al., 2020; Schaller and Ehlers, 2022), and through its influence on physical and chemical weathering processes, as well as glacial, fluvial and hillslope erosion (e.g. Valla et al., 2011; Herman et al., 2013; Lease and Ehlers, 2013; Perron, 2017). Climate change from the Late Cenozoic to present has played an important

role in eroding mountain topography and lowland sedimentation (Hasler et al., 2011; Herman and Champagnac, 2016; Marshall et al., 2015; Peizhen et al., 2001; Rangwala and Miller, 2012). Climate change influences surface processes through not only precipitation changes, but also through seasonal temperature changes that affect physical weathering mechanisms, such as frost cracking (Anderson, 1998; Delunel et al., 2010; Hales and Roering, 2007; Walder and Hallet, 1985). Critical cracking occurs when the pressure of freezing (and expanding) water in pore walls or fractures exceeds the cohesive strength of the porous media and causes cracks to propagate (Davidson and Nye, 1985). However, subcritical cracking can also occur without exceeding thresholds (Eppes and Keanini, 2017). Frost cracking is a dominant mechanism of weathering in periglacial regions (Marshall et al., 2015), and typically occurs at latitudes greater than 30°N and 30°S or in high elevations.

Previous field studies of frost cracking in mountain regions includes studies in, for example, the Japanese Alps (Matsuoka, 2001), Southern Alps of New Zealand (Hales and Roering, 2009), Swiss Alps (Amitrano et al., 2012; Girard et al., 2013; Matsuoka, 2008; Messenzehl et al., 2017), French Western Alps (Delunel et al., 2010), Italian Alps (Savi et al., 2015), Eastern Alps (Rode et al., 2016), Austrian Alps (Kellerer-Pirklbauer, 2017), Oregon (Marshall et al., 2015; Rempel et al., 2016), and the Rocky Mountains, USA (Anderson, 1998). These studies demonstrated clear relationships between changes in near surface air temperatures and frost cracking. Various models have also been developed to estimate frost cracking intensity (FCI) using mean annual air temperatures (MAT) (Andersen et al., 2015; Anderson, 1998; Anderson et al., 2013; Hales and Roering, 2007; Marshall et al., 2015) and in some cases, with the additional consideration of sediment thickness variations over bedrock (Andersen et al., 2015; Anderson et al., 2013). These studies document the importance of time spent in the frost cracking window (FCW) for the frost-cracking intensity (FCI) of a given area. The assumption of FCW is based on the premise that frost cracking occurs in response to segregation ice growth in bedrock when subsurface temperatures are between -8 °C and -3 °C (Anderson, 1998). However, this assumption is not supported by physical models (e.g. Walder and Hallet, 1985), field data (e.g. Girard et al., 2013; Draebing et al., 2017) or lab simulations (e.g. Murton et al., 2016). The FCW depends on rock strength and crack geometry (Walder and Hallet, 1985), and thus spatial variations are expected due to lithological changes. More complex models consider near surface thermal gradients as a proxy of the frost cracking intensity for segregation ice growth, as well as the effects of overlying sediment layer thickness on frost cracking (Andersen et al., 2015).

The previous studies provide insight into not only observed regional variations in frost cracking, but also some of the key processes required for predicting frost cracking intensity. However, despite recognition that Late Cenozoic global climate change impacts surface processes (e.g. Mutz et al., 2018; Mutz and Ehlers, 2019) and frost-cracking intensity (e.g. Marshall et al., 2015), to the best of our knowledge, no study has taken full advantage of climate change predictions in conjunction with a process-based understanding of the spatiotemporal variations in frost cracking on a global scale. This study builds upon previous work by estimating the global response in FCI to different end-member climate states. Here, we complement previous work on the effects of climate on surface processes by addressing the following hypothesis: If Late Cenozoic global climate change resulted in latitudinal variations in ground surface temperatures, then the intensity of frost cracking should temporally and spatially vary in such a way that leads to the occurrence of more intense frost cracking at lower latitudes during colder climates. We do this by coupling existing frost-cracking models to high-resolution paleoclimate General Circulation Model (GCM) simulations (Mutz et al., 2018). More specifically we apply three different frost-cracking models that are driven by predicted surface temperature changes from GCM time-slice experiments including (a) the Pliocene

76 (~3 Ma, PLIO), considered an analog for Earth's potential future due to anthropogenic climate change, (b) the

77 Last Glacial Maximum (~21 ka, LGM), covering a full glacial period, (c) the Mid-Holocene (~6 ka, MH) climate

78 optimum, and (d) Pre-Industrial (~1850 CE, PI) conditions before the onset of significant anthropogenic

79 disturbances to climate.

80 2. Data

81 This manuscript builds upon, and uses, paleoclimate model simulations we previously published for different time

82 periods (Mutz et al., 2018; Mutz and Ehlers, 2019). The output from those simulations was used for new

83 calculations of FCI described below. More specifically, the climate and soil dataset used for this study includes

84 simulated daily land surface temperatures (obtained from the Mutz et al. (2018) simulations) for different

85 paleoclimatic time-slice experiments (PI, MH, LGM and PLIO) conducted with the GCM ECHAM5 simulations,

86 and soil thickness data (Wieder, 2014). Due to the lack of paleo soil thickness data, global variations in soil

87 thickness are assumed to be uniform between all time-slices investigated. The reader is advised that this

88 assumption has limitations and would introduce uncertainty in the model results as past weathering would alter

89 soil thickness and hence influence further weathering. However, as the main goal of this study is to simulate and

90 analyze the climate change effect for global FCI changes in different palaeoenvironmental conditions, we keep

91 the soil thickness constant. In addition, there are no data sets available for past soil thicknesses that would allow

92 circumventing the approach used here. Given this, we use a present-day dataset for soil thickness due to the

93 absence of paleo soil data.

94 The ECHAM5 paleoclimate simulations were conducted at a high spatial resolution (T159, corresponding roughly

95 to a 80km x 80km horizontal grid at the equator) and 31 vertical levels (to 10hPa). ECHAM5 was developed at

96 the Max Planck Institute for Meteorology (Roeckner et al., 2003). It is based on the spectral weather forecast

97 model of ECMWF (Simmons et al., 1989) and is a well-established tool in modern and paleoclimate studies. The

98 ECHAM5 paleoclimate simulations by Mutz et al. (2018) were driven with time-slice specific boundary

99 conditions derived from multiple modeling initiatives and paleogeographic, paleoenvironmental and vegetation

100 reconstruction projects (see Table 1). Details about the boundary conditions and prevailing climates for specific

101 time-slices (PI, MH, LGM and PLIO) are provided in Mutz et al. (2018). Each simulated time-slice resulted in 17

102 simulated model years, where the first two years contained model spin up effects and were discarded. The

103 remaining 15 years of simulated climate were in dynamic equilibrium with the prescribed boundary conditions

104 and used for our analysis.

105

106

107

108

109

110

111

112

Table 1. Boundary Conditions of the paleoclimate simulations (Mutz et al., 2018).

Paleoclimate Simulations	Boundary Conditions
PI (~ 1850)	• Sea-Surface temperatures (SST) and sea-ice concentrations (SIC) were sourced from transient coupled ocean-atmosphere simulations (Dietrich et al., 2013; Lorenz and Lohmann, 2004) • Green-house gas (GHG) concentrations (Dietrich et al., 2013) were obtained from ice-core-based reconstructions of CO_2 (Etheridge et al., 1996), CH_2 (Etheridge et al., 1998), and N_2O (Sowers et al., 2003)
MH (~ 6 ka)	• SST and SIC are derived from a transient, low resolution, coupled atmosphere-ocean simulation of the mid (6 ka) Holocene (Lohmann et al., 2013; Wei and Lohmann, 2012) • GHG concentrations (Dietrich et al., 2013) are obtained from ice-core-based reconstructions of CO_2 (Etheridge et al., 1996), CH_2 (Etheridge et al., 1998), and N_2O (Sowers et al., 2003) • Global vegetation maps are based on plant functional types maps by the BIOME 6000 / Palaeovegetation Mapping Project (Prentice et al., 2000; Harrison et al., 2001; Bigelow et al., 2003; Pickett et al., 2004) and model predictions by Arnold et al. (2009) • Orbital parameters from Dietrich et al., (2013)
LGM (~ 21 ka)	• Land-sea distribution and ice sheet extent and thickness are based on the PMIP III guidelines (Abe-Ouchi et al., 2015) • SST and SIC are based on GLAMAP (Sarnthein et al., 2003) and CLIMAP (CLIMAP group members, 1981) reconstructions • GHGs concentrations are prescribed following Otto-Bliesner et al. (2006) • Global vegetation maps are based on plant functional types maps by the BIOME 6000 / Palaeovegetation Mapping Project (Prentice et al., 2000; Harrison et al., 2001; Bigelow et al., 2003; Pickett et al., 2004) and model predictions by Arnold et al. (2009) • Orbital parameters from Dietrich et al., (2013)
PLIO (~ 3 Ma)	• Surface conditions (SST, SIC, sea land mask, topography and ice cover), GHG concentrations and orbital parameters are obtained from the PRISM project (Haywood et al., 2010; Sohl et al., 2009; Dowsett et al., 2010) • PRISM vegetation reconstruction converted to ECHAM5 compatible plant functional types following Stepanek and Lohmann (2012)

* (SST: Sea Surface Temperature; SIC: Sea Ice Concentration; GHG: Greenhouse Gas; PMIP III: Paleoclimate Modelling Intercomparison Project, phase 3; PRISM: Pliocene Research, Interpretation and Synoptic Mapping)
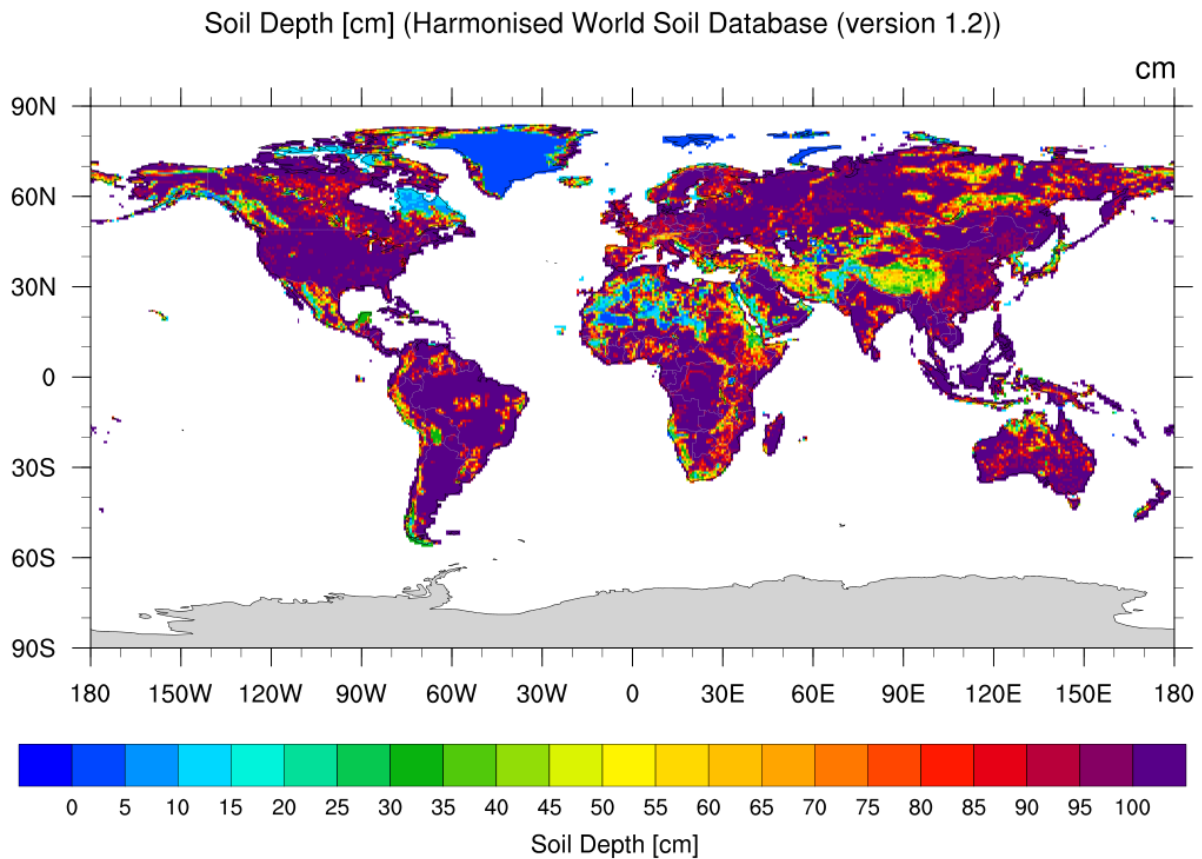
Figure 1. Soil depth map from the Harmonized World Soil Databased (HWSD, version 1.2) used in this study (Wieder, 2014). Due to the paucity of some data inputs for paleoclimate time-slices (e.g. soil thickness, rock properties, hydrology, etc.), the simulations assume present day values.

Soil thickness data was obtained from the re-gridded Harmonized World Soil Database (HWSD) v1.2 (Wieder, 2014) which has a 0.05-degree spatial resolution and depths ranging from 0 *m* to 1 *m* (Fig. 1). The above soil thickness data was upscaled to match the spatial resolution of the ECHAM5 paleoclimate simulations (T159, ca. 80km x 80km).

3. Methods

In this section we present the pre-processing of GCM paleo-temperature data for the calculation of mean annual temperatures (MAT) and the half amplitude of annual temperature variations (Ta). This is followed by the description of the models (simpler to complex) that were applied to generate first order (global) estimation of annual depth integrated FCI for selected Cenozoic time-slices.

3.1. Pre-processing of GCM simulation temperature data

We calculated the mean annual land surface temperatures (MAT) to serve as input for subsequent calculations and a reference for differences in global paleoclimate. The MAT's for the paleoclimate GCM experiments (PLIO, LGM, MH, and PI) were calculated (Fig. 2) from each of the simulations' 15 years of daily land surface

temperature values. In addition, the half amplitude of annual surface temperature variations (Ta) was extracted at all surface grid locations for all years (Fig. 3). We use the MAT for ground surface temperature in subsequent calculations, following Anderson et al., (2013), Marshall et al., (2015), and Rempel et al., (2016) . The maxima and minima for global average MAT's and Ta's for all the time-slices are shown in Table 2.
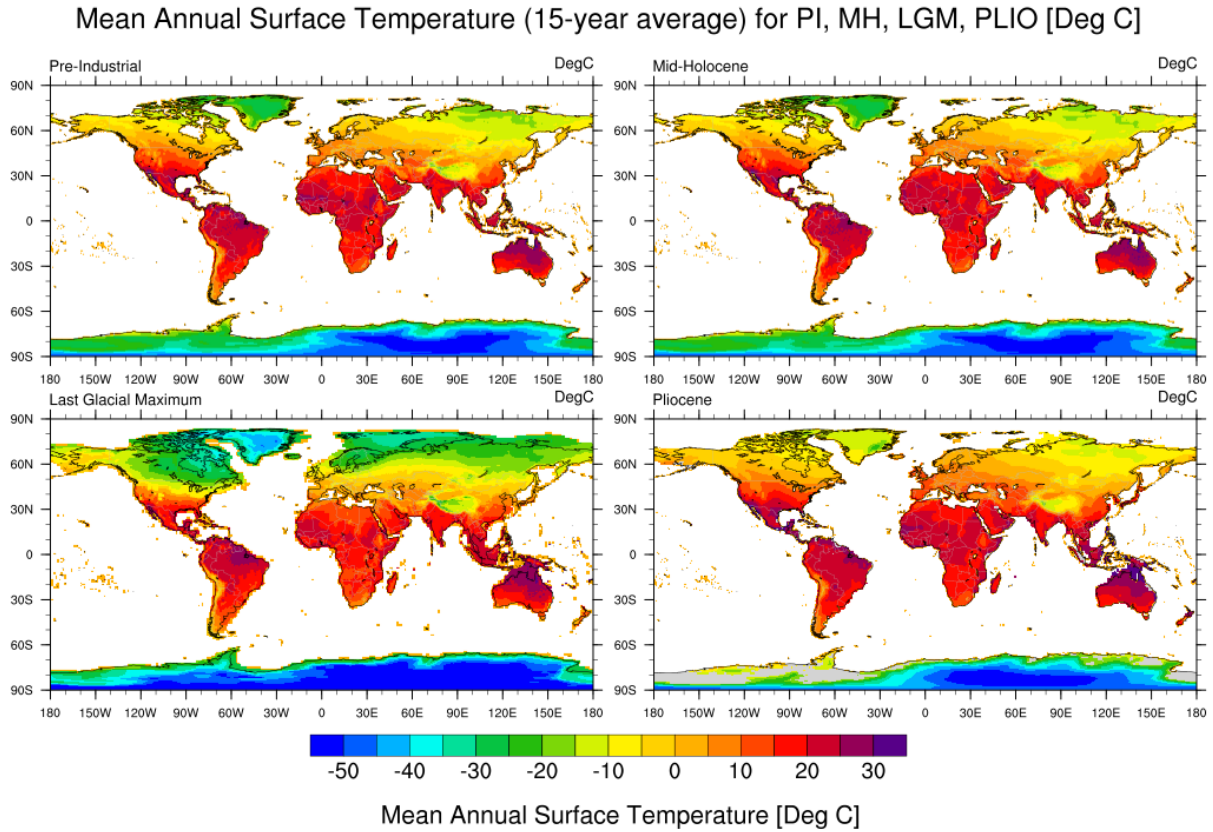
Figure 2. Mean Annual Surface Temperature maps (15-year average) from the ECHAM5 GCM simulations for the Pre-Industrial (top-left), Mid-Holocene (top-right), Last Glacial Maximum (bottom-left), and mid-Pliocene (bottom-right) (unit: °C). These are calculated from GCM simulation output of Mutz et al. (2018) and Mutz and Ehlers (2019).

Table 2. MAT and Ta (for ground surface temperature) for Pre-Industrial, Mid-Holocene, Last Glacial Maximum and Pliocene simulations.

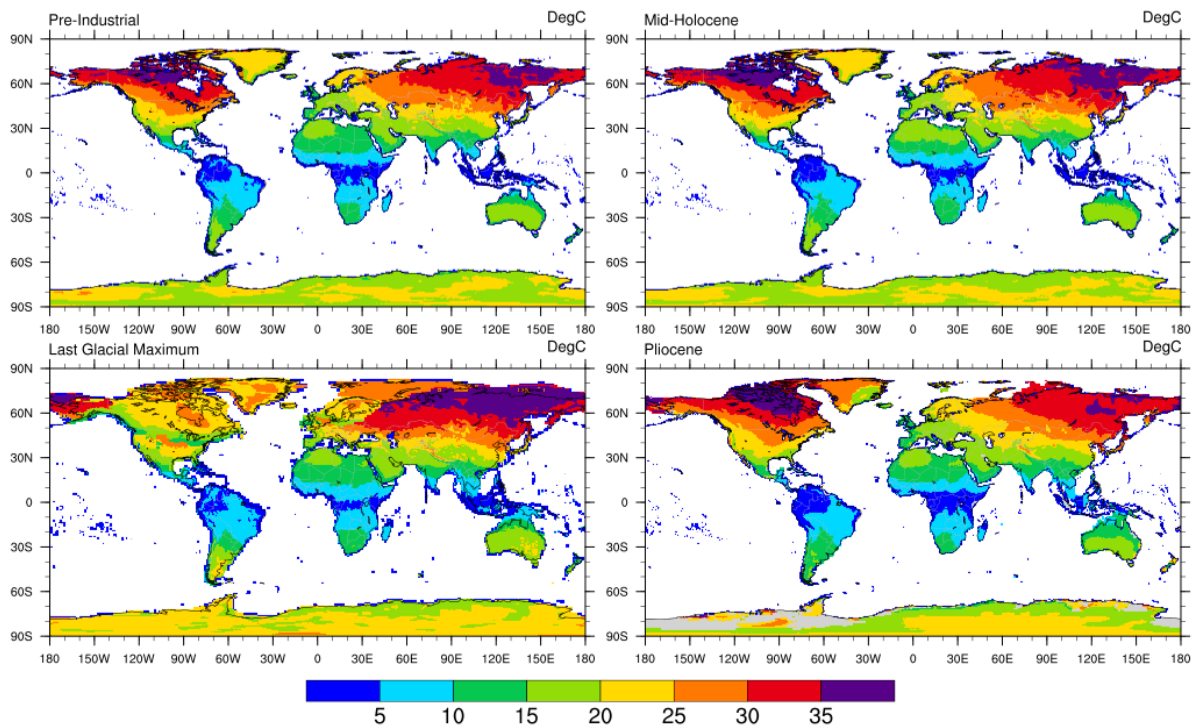| Time-slices (Paleoclimate Simulations)	MAT (°C)		Ta (°C)	
	Minimum	Maximum	Minimum	Maximum
Pre-Industrial (~ 1850)	-58	34	0	39
Mid-Holocene (~ 6 ka)	-58	35	0	40
Last Glacial Maximum (~21 ka)	-67	39	0	42
Pliocene (~ 3 Ma)	-56	48	0	43

The calculation of temporally varying sub-surface temperatures follows the approach of Hales and Roering (2007) and uses the analytical solution for the one-dimensional heat conduction equation (Turcotte and Schubert, 2014)

forced with daily temperatures following sinusoidal variations. While daily paleo-temperatures can be obtained from Mutz et al. (2018), the daily variations produced by the GCM cannot be validated as well as seasonal or annual means. To avoid overinterpretation of the GCM simulations, we refrained from using daily paleo-temperatures from Mutz et al. (2018) and instead use sinusoidal daily temperatures. Temperature variations with depth and time were calculated at each GCM grid point as:

$$T(z,t) = MAT + Ta \cdot e^{-z\sqrt{\frac{\pi}{\alpha P_y}}} \cdot sin\left(\frac{2\pi t}{P_y} - z\sqrt{\frac{\pi}{\alpha P_y}}\right) \tag{1}$$

where, T represents daily subsurface temperature at depth z (m) and time t (days in a year), MAT and Ta represent mean annual surface temperature and half amplitude of annual temperature variation respectively, P_y is the period of the sinusoidal cycle (1 year), and α is the thermal diffusivity. Thermal diffusivity values near the Earth's surface can range from $1 - 2 \times 10^{-6} m^2 s^{-1}$ for most rocks (Anderson, 1998) and range between $7 - 10 \times 10^{-7} m^2 s^{-1}$ for other Earth materials comprising the overlying sediment layer (Eppelbaum et al., 2014). In this study, we used a thermal diffusivity of $1.5 \times 10^{-6} m^2 s^{-1}$ for bedrock and $8 \times 10^{-7} m^2 s^{-1}$ for the overlying sediment layer. The maximum depth investigated here is 20 m, as it is slightly deeper than the maximum frost penetration depth of ~14 m reported by (Hales and Roering, 2007).
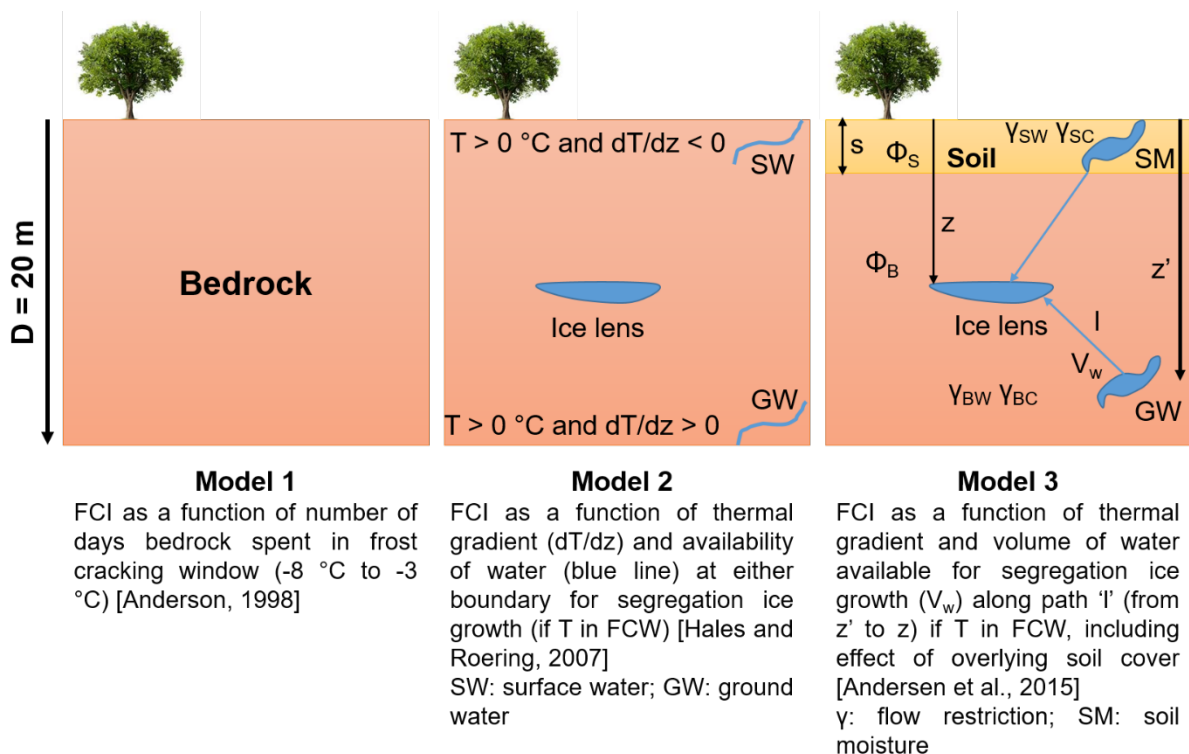

Figure 3. Half Amplitude of Annual Temperature Variation (15-year average) for the Pre-Industrial (top-left), Mid-Holocene (top-right), Last Glacial Maximum (bottom-left), and Pliocene (bottom-right) (unit: °C). These are calculated from GCM simulation output of Mutz et al., (2018) and Mutz and Ehlers (2019).

The calculation of subsurface temperatures was discretized into 200 depth intervals from the surface to the maximum depth of 20 m. Smaller depth intervals (~1 cm) were used near the surface and large intervals (~20 cm) at greater depths, because the FCI is expected to change most dramatically near the surface and dampen with depth due to thermal diffusion (Andersen et al., 2015).

3.2.   Estimation of Frost Cracking Intensity

We applied three different approaches (models) with different levels of complexity to estimate global variations in frost cracking during different past climates (Fig 4; Andersen et al., 2015; Anderson, 1998; Hales and Roering, 2007). The models use predicted ground surface temperatures from each grid cell in the GCM to calculate subsurface temperatures and FCI. We then calculate differences between the FCI from the PI reference simulation and the FCI predicted for the PLIO, LGM and MH time-slices to assess relative change in FCI over the Late Cenozoic. The conceptual diagram (Fig. 4) illustrates differences in the models used in our study, which are discussed in detail in sections 3.2.1 - 3.2.3. Models 1-3 successively increase in complexity and consider more factors. The approach of Andersen et al., (2015), referred to here as Model 3, is the most recent and complex in its consideration of the processes (e.g. effect of soil-cover on FCI) that are relevant for frost cracking. Given this, we focus our presentation of results in the main text here on Model 3, but for completeness describe below differences of Model 3 from earlier Models (1-2). For brevity, results from the earlier models are presented in the supplementary material. A flowchart illustrating our methods is presented in Fig. 5. Similar to previous studies, the hydrogeological properties of the bedrock (i.e. infiltration, water saturation, porosity and permeability) are ignored in this study. This approach provides a simplified means for estimating the FCI for underlying bedrock at a global scale.

**Model 1**
FCI as a function of number of days bedrock spent in frost cracking window (-8 °C to -3 °C) [Anderson, 1998]

Model 2
FCI as a function of thermal gradient (dT/dz) and availability of water (blue line) at either boundary for segregation ice growth (if T in FCW) [Hales and Roering, 2007]
SW: surface water; GW: ground water

Model 3
FCI as a function of thermal gradient and volume of water available for segregation ice growth (V_w) along path 'l' (from z' to z) if T in FCW, including effect of overlying soil cover [Andersen et al., 2015]
γ: flow restriction; SM: soil moisture

188 **Figure 4. Conceptual diagram of the models (1, 2, and 3) used for estimating FCI (T: temperature; dT/dz: thermal**
189 **gradient; SW: surface water; GW: groundwater; SM: soil moisture; s: sediment thickness; φS: soil porosity (0.02); φB:**
190 **bedrock porosity (0.3)).**
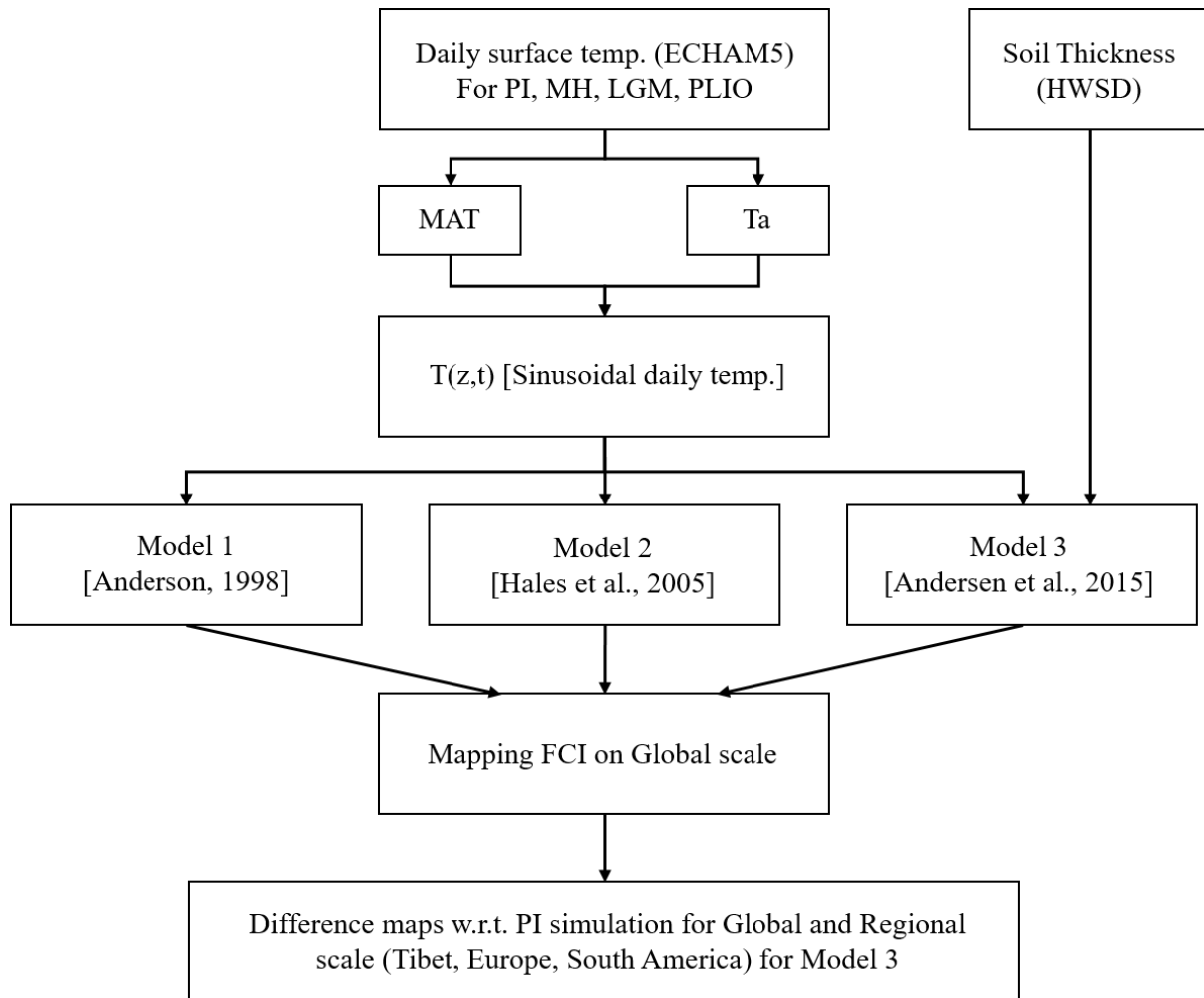
191

192 **Figure 5. Flowchart describing the methods used in the study based on daily surface temperature simulated by the**
193 **ECHAM GCM. and soil thickness data from HWSD v1.2. Abbreviations include: MAT - mean annual temperature;**
194 **Ta - half amplitude of annual temperature variation; T (z, t) - subsurface temperature at depth *z* and time *t*; FCI - frost**
195 **cracking intensity.**

196 **3.2.1.   Model 1: Frost cracking intensity as a function of time spent in the frost cracking window (FCW)**

197   Model 1 represents the simplest approach and applies the method of Anderson (1998). In our application of this
198   model, we use a more representative thermal diffusivity value for rocks of $1.5 \times 10^{-7} m^2 s^{-1}$, because the
199   previous study was specific to granitic bedrock and applied a diffusivity specific to that. Furthermore, the
200   boundary conditions of a low rock surface albedo (≤ 0.1) and presence of a high atmospheric transmissivity ($\geq$
201   0.9) on the surface were relaxed, as surface temperatures were used in our study instead of near-surface air
202   temperatures.

For our implementation of model 1, we applied equation 1 for sinusoidal varying daily temperatures at the surface, and calculated temperatures up to 20 m depth. The number of days spent in the FCW (-8 °C to - 3 °C) for each depth interval were calculated over a period of 1 year for all time slices (PI, MH, LGM and PLIO):

$$FCI(z) = \begin{cases} N(z), if -8°C < T(z,t) < -3°C \\ 0, else \end{cases} \tag{2}$$

where *FCI (z)* is referred to the frost cracking intensity at depth *z*. *N (z)* indicates the number of days the bedrock (at depth z) spends in the FCW over a period of 1 year.

Estimation of frost cracking intensity for each location included depth averaging of the FCI such that:

$$\acute{FCI} = \frac{1}{D} \int_0^D FCI(z) dz \tag{3}$$

where $\acute{FCI}$ is the integrated frost cracking intensity to a depth of *D = 20 m*. The unit of integrated frost cracking intensity in this model is $Days$. The FCI values are calculated for all model years separately and then averaged over the total time (15 years) for each paleoclimate time-slice.

3.2.2. Model 2: Frost cracking intensity as a function of subsurface thermal gradients

Model 2 applies the approach of Hales and Roering (2007) to estimate FCI using climate change driven variations in subsurface thermal gradients. This approach extends the work of Anderson (1998) with the additional consideration of segregation ice growth. Segregated ice growth is attributed to the migration of liquid water to colder regions in shallow bedrock, accumulating in localized zones to form ice lenses inducing weathering (Walder and Hallet, 1985).

To facilitate ice segregation growth, the model assumes the availability of liquid water (T > 0 °C) at either boundary (z = 0 *m* or z = 20 *m*), with a negative thermal gradient for a positive surface temperature, and a positive thermal gradient for the positive lower boundary (z = 20 m) temperature. This implementation supports frost cracking in the bedrock with temperatures between – 8 °C and – 3 °C (Hallet et al., 1991). In the case of permafrost areas, MAT is always negative, but as sinusoidal T(z, t) is calculated based on MAT and Ta, a positive T (> 0 °C) may occur during warmer days of the year. In addition, Ta is higher for higher latitudes (Fig. 3), which are more prone to frost cracking.

The model is described as follows:

$$FCI(z,t) = \begin{cases} \left|\frac{dT}{dz}\right|(z,t), if -8°C < T(z,t) < -3°C \\ 0, else \end{cases} \tag{4}$$

$$\acute{FCI} = \int_0^D \int_0^{Py} FCI(z,t) \, dtdz \tag{5}$$

where *FCI (z, t)* is the frost cracking intensity at depth *z* and time *t*. It is an index for the absolute value of the thermal gradient at that particular depth and time that fulfils the conditions defined above.

In equation 5, $\acute{FCI}$ represents the integrated FCI for a geographic location. More specifically, the FCI is integrated over one year at each depth and then integrated for all depth elements. *D* represents depth (20 m), *Py* is a period

234 of the sinusoid (1 year), dt is the time interval (1 day) and dz is the depth interval, as described in section 3.1. The

235 unit of integrated frost cracking intensity in this case is °C.

3.2.3. Model 3: Frost cracking intensity as a function of thermal gradients and sediment thickness

237 In the final (most complex) approach used in this study, the effect of an overlying soil layer (Fig. 1) is considered

238 in addition to the subsurface thermal gradient variations with depth. This model applies the approach of Andersen

239 et al. (2015), which extends the work of Hales and Roering (2007) and Anderson et al. (2013). The model

240 assumptions are similar to the previous approaches. For segregation ice growth, it additionally considers the

241 influence of the volume of water available in the proximity of an ice lens. The parameters used in Model 3 are

242 listed below (Table 3).

243 **Table 3. Input parameters for Model 3 *(Andersen et al., 2015)***

Symbol	Description	Value
Φ_S	Porosity of soil	0.3
Φ_B	Porosity of bedrock	0.02
γ_{SW}	Flow restriction in warm soil	1.0 m^{-1}
γ_{SC}	Flow restriction in cold soil	2.0 m^{-1}
γ_{BW}	Flow restriction in warm bedrock	2.0 m^{-1}
γ_{BC}	Flow restriction in cold bedrock	4.0 m^{-1}
V_{CW}	Critical water volume	0.04 m

244

245 In Model 3, frost cracking intensity is estimated as a product of the thermal gradient and volume of water available

246 (V_W) for segregation ice growth at each depth element, such that:

247 $$FCI(z,t) = \begin{cases} \left|\frac{dT}{dz}(z,t)\right| V_W(z), if -8°C < T(z,t) < -3°C \\ 0, else \end{cases} \tag{6}$$

248 where, FCI (z, t) is the frost cracking intensity in bedrock at depth z and time t, and V_W (z) is the volume of water

249 available for segregation ice growth. V_W (z) is estimated at each depth (z) by integrating the occurrence of unfrozen

250 water along a path l, starting at depth z and following a positive thermal gradient towards the ice lens. The volume

251 of available water ($V_W(z)$) and total flow restriction ($\Gamma(z')$), between the depth of occurrence of water (z') and the

252 location of segregation ice growth (z), are calculated using equations 7 and 8 respectively (Andersen et al., 2015):

253 $$V_W(z) = \int_l \phi(z') w_f(z') e^{-\Gamma(z')} dz' \tag{7}$$

254 $$\Gamma(z') = \int_z^{z'} \gamma(z'') dz'' \tag{8}$$

255 where, l is the distance from depth z to the surface, lower boundary, or an interface where the thermal gradient

256 changes sign (from positive to negative or vice versa). The penalty function $e^{-\Gamma(z')}$ (Anderson et al., 2013) is a

257 function of the total flow restriction ($\Gamma(z')$) at the depth z'. Since segregation ice growth is exhibited at sub-zero

258 temperatures (below – 3℃) and liquid water is available at positive temperatures (T > 0℃), water must migrate

259 through a mixture of frozen and unfrozen soil or the bedrock. The variables γ_{SW}, γ_{SC}, γ_{BW}, γ_{BC} (defined in Table

260 3) represent the flow restriction parameters and were used in the model to approximate a range of permeabilities

261 (Andersen et al., 2015), but do not explicitly simulate water transport. However, it is unclear if the inclusion of

262 the penalty function leads to a better representation of frost cracking processes. Therefore, we conducted two sets

263 experiments for Model 3 that were conducted with, and without, the penalty function and are presented in section

264 4.1 and 4.2, respectively.

265 The soil porosity ($\varphi_S = 0.3$) is assumed to be higher than that of bedrock ($\varphi_B = 0.02$). V_W (z) is expected to be high

266 due to the presence of unfrozen soil in the proximity of a frozen bedrock. Since Model 3 limits the positive effects

267 of V_W to a critical water volume V_{CW} (Table. 2, i.e., if $V_W > V_{CW}$, then $V_W = V_{CW}$), the expected high ($> V_{CW}$)

268 values for V_W will not affect frost cracking any further.

269 Lastly, the integrated frost cracking intensity $\acute{FCI}$ across Earth's terrestrial surface was calculated by depth

270 integration of the FCI averaged over a period of 1 year (Anderson et al., 2013):

271 $$\acute{FCI} = \frac{1}{Py} \int_0^{Py} \int_0^D FCI(z,t)\,dz\,dt \tag{9}$$

272 where, Py is 1 year and D is the maximum depth investigated (20 m). The unit of integrated FCI in this model is

273 ℃m. Integrated FCI is calculated for each of the GCM simulation's model years and then averaged over the

274 total number of years (15 years).

4. Results

276 In the following, we document the general trends in the estimated FCI from Model 3 (Andersen et al., 2015) for

277 all the paleoclimate time-slices (PI, MH, LGM, PLIO) based on the coupling of the above models to GCM output

278 for these time slices. We present the results for the experiments conducted with and without the penalty function

279 separately in sections 4.1 and 4.2, respectively. The FCI distribution is masked for the glaciated regions during

280 specific paleoclimate time-slices, as the surface covered under ice-sheets is disconnected from atmospheric

281 processes (Grämiger et. al. 2018). In the PLIO results, the regions that experienced Pleistocene glaciation are

282 masked with the LGM glacier cover, as the assumption of comparable soil depths in these regions is heavily

283 violated. Since spatial and temporal variations in frost cracking do not vary much between the three approaches,

284 for brevity we focus our presentation of results on the most recent (Model 3 - Andersen et al., 2015) approach.

285 The results of simpler approaches (Model 1, 2; Anderson 1998 and Hales and Roering, 2007) are presented in the

286 supplementary material.

4.1. Model 3 - Scenario 1: FCI as a function of thermal gradient and soil thickness (with penalty function)

289 In this scenario, we estimate the global FCI distribution using Model 3 (Andersen et al., 2015) with the penalty

290 function, which makes FCI dependent on the distance to water. The predicted global sum of FCI is greatest for

291 the MH (~31,3997 °C m), followed by the PI (~30,3235 °C m), LGM (~23,8277 °C m) and PLIO (~21,6529 °C

292 m). The correlation between FCI values and Ta is high (Pearson r: between 0.8 and 0.89) and statistically

293 significant (using the 95% level as a threshold to determine significance). On the other hand, the correlation

between FCI and MATs is good in the LGM (Pearson r: -0.68), moderate in the PI and MH (Pearson r: -0.3 – -0.4), and poor in the PLIO (Pearson r: -0.04).

For all paleoclimate time slice experiments, the FCI predicted by Model 3 is in the range of $0 – 0.22$ °C m at higher latitudes (30 °N – 80 °N and 45 °S – 60 °S) (Fig. 6). The maximum FCI values are observed in the higher latitudes (50 °N – 80 °N) and show the same pattern as variations in Ta when Ta exceeds 30°C. In the PI and MH simulations, the highest FCI is observed in North America (40°N – 55°N and 70°N – 80°N) and Eurasia (35 °N – 50 °N, 55 °E – 80 °E and 55 °N – 80 °N, 80 °E – 180 °E), with values ranging from ~0.08 °C m to ~0.2 °C m. Low FCI can be observed in South America, with values between 0.02 °C m and 0.05 °C m. This is consistent with results from models 1 and 2 (see supplement). In the LGM simulation, the highest FCI values are observed in Alaska, Turkmenistan, Uzbekistan, Eastern China and north-eastern latitudes in Eurasia (70 °N – 80 °N, 105 °E – 180 °E) with values ranging from ~0.08 °C m to ~0.2 °C m. In the Andes of South America, the frost cracking activity is restricted to the geographical range of 12 °S – 55 °S. The highest South American FCI values (~ 0.15 °C m to ~ 0.22 °C m) are predicted for the southern part of the continent (40 °S – 50 °S).
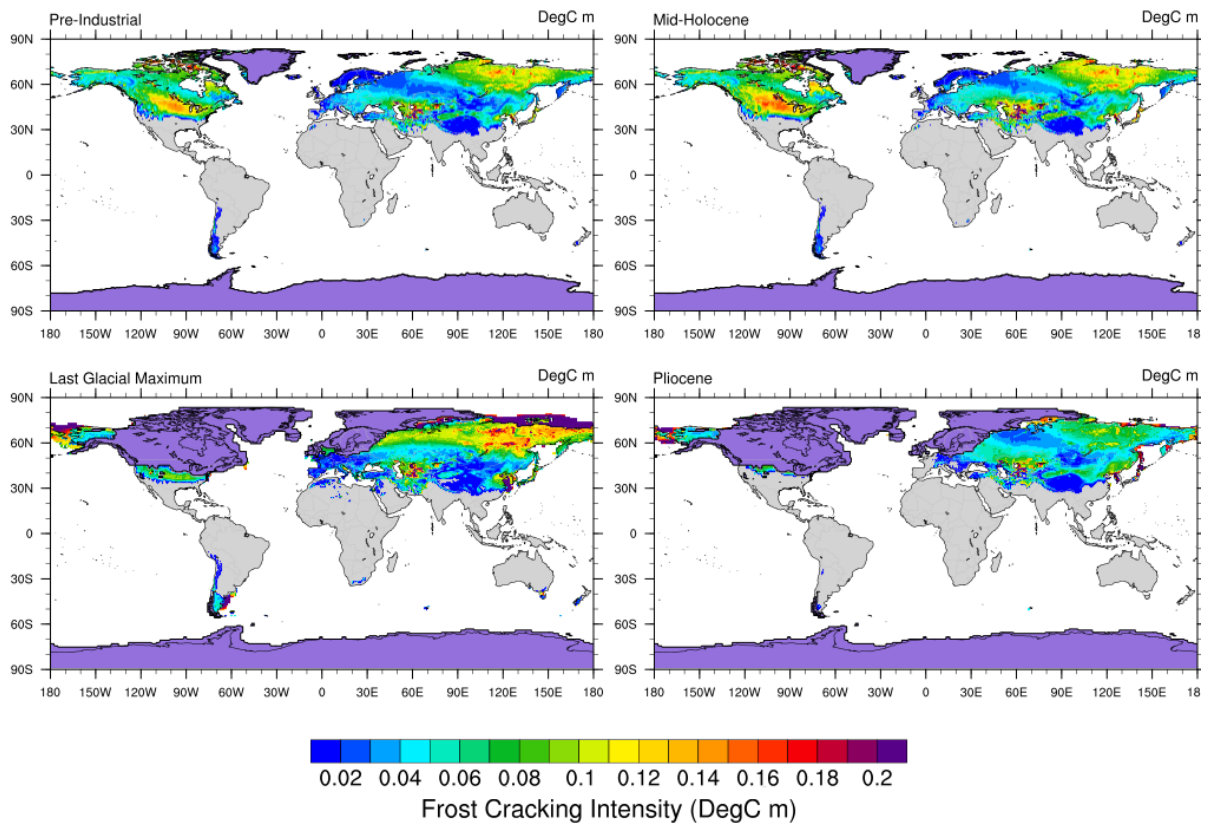
Figure 6. Model 3 (Scenario 1) predicted integrated FCI as a function of thermal gradient and sediment thickness (with the penalty function) for Pre-Industrial (top-left), Mid-Holocene (top-right), Last Glacial Maximum (bottom-left), and mid-Pliocene (bottom-right) times (unit: °C m). The grey areas in plots indicates the absence of frost cracking. For all time slices, the regions covered by ice were removed from the calculation and are highlighted in violet color (Bracannot et al., 2012). For the PLIO results, the LGM ice cover is used, since the assumption of modern soil depth is heavily violated in these regions.

In the mid-Pliocene, the maximum FCI values are predicted in the higher latitudes i.e., Alaska (~0.15 °C m - ~0.22 °C m). Moderately high values are predicted for the northern latitudes of Eurasia (0.05 °C m – 0.16 °C m). Overall,

13

316   the magnitude of mid-Pliocene FCI is lower than that of all other investigated time slices. The only exceptions are

317   some high-latitude regions (e.g. Alaska) that exhibit locally higher FCI values in the mid-Pliocene relative to the

318   PI. Negligible frost cracking is predicted for South America, which is consistent with the results of Model 1

319   (Anderson, 1998).

320   For all the time-slices, regions with positive MATs (0 °C to 15 °C) exhibit higher values of FCI where the sediment

321   cover is thinner (e.g. Middle East Asia). In contrast, predictions of FCI in regions with negative MATs (-5 °C to

322   -20 °C) and high Ta (30 °C to 40 °C) tend to be higher where sediment cover is thicker (e.g. North East Eurasia).

323   **4.2.**   **Model 3 - Scenario 2: FCI as a function of thermal gradient and soil thickness (without penalty**
324   **function)**

325   In this scenario, we estimate global FCI distribution using Model 3 (Andersen et al., 2015) without applying the

326   penalty function (Fig. 7). The highest magnitude of frost cracking intensity is simulated for the PLIO (~53 °C m),

327   followed by the MH (~47 °C m), PI (~45 °C m), and LGM (~43 °C m). However, the maximum global sum of

328   FCI is observed in the MH (~31,3997 °C m), followed by the PI (~30,3235 °C m), LGM (~23,8277 °C m) and

329   PLIO (~21,6529 °C m) simulations. Similar to the observations in Model 2 (see Supplement S.2), the FCI

330   distribution is negatively correlated with MATs (Pearson r: between -0.4 and -0.5) and Ta (Pearson r: between

331   0.9 and 0.95). These correlations are significant (using the 95% threshold to determine significance).

332   In the PI simulations, the maximum FCI values are predicted for the mid-high latitudes (i.e., FCI: 21 – 44 °C m

333   in 40 °N – 70 °N) of North America and Eurasia. Low to moderate frost cracking is predicted for South America

334   (i.e., FCI: 6 – 18 °C m in 20 °S – 55 °S). The MH simulations predict a similar FCI pattern and   FCI values that

335   are slightly higher than in the PI (e.g., FCI: 21 – 47 °C m in 40 °N – 70 °N).

336   In the LGM simulation, major portions of North America and Europe are covered by ice-sheets and thus excluded

337   from our frost cracking models. The simulations yield maximum FCI values for Alaska (i.e. 21 – 44 °C m) and

338   the mid-high latitudes in Asia (i.e. FCI: 14 – 42 °C m in 35 °N – 65 °N), moderate FCI values in the peri-glacial

339   regions in North America (i.e. FCI: 18 – 33 °C m in 35 °N – 42 °N), and low FCI values in South America (i.e.

340   FCI: 4 – 18 °C m in 15 °S – 55 °S). In the PLIO simulation, major frost cracking activity is predicted for Alaska

341   (i.e. 21 – 48 °C m) and the northern latitudes of Asia (i.e. FCI: 18 – 48 °C m in 30 °N – 80 °N). We do not observe

342   any significant frost cracking in Europe, North America and South America in the PLIO simulations.
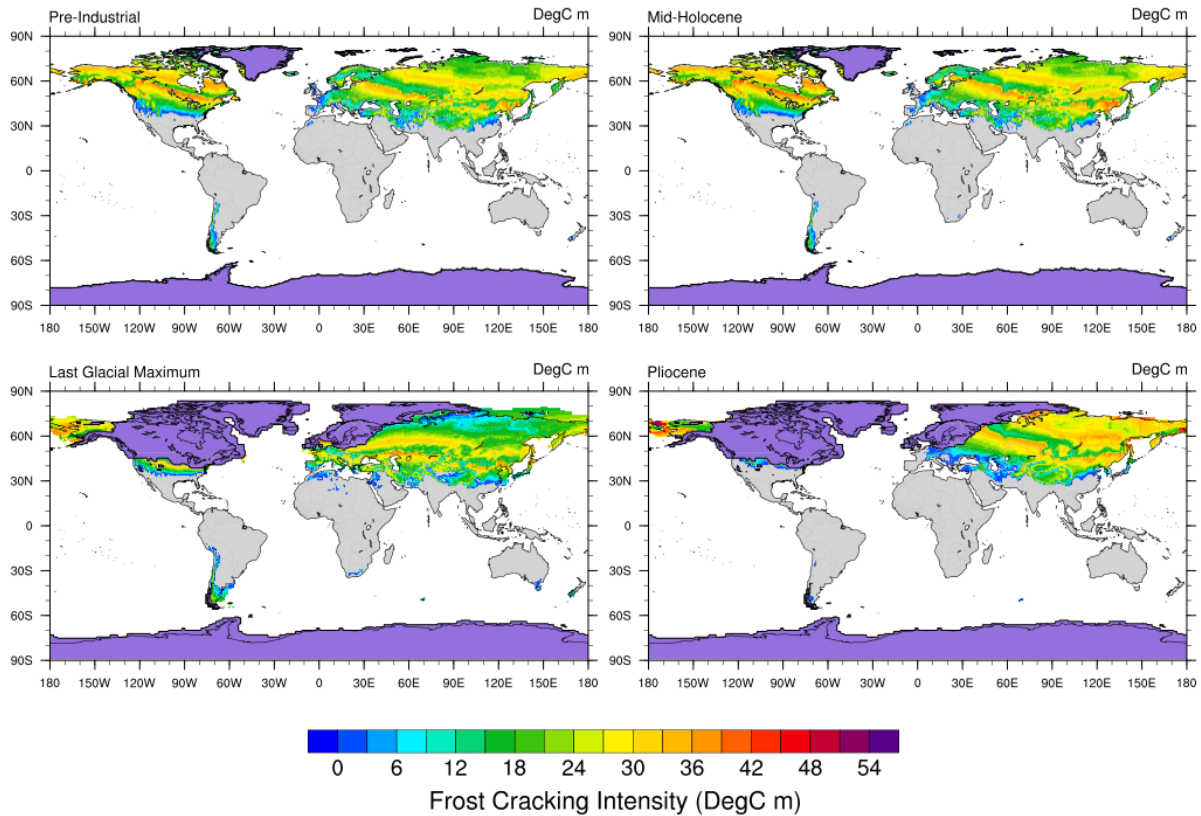
Figure 7. Model 3 (Scenario 2) predicted integrated FCI as a function of thermal gradient and sediment thickness (without the penalty function) for Pre-Industrial (top-left), Mid-Holocene (top-right), Last Glacial Maximum (bottom-left), and mid-Pliocene (bottom-right) times (unit: °C m). The grey areas in plots indicates the absence of frost cracking. For all time slices, the regions covered by ice were removed from the calculation and are highlighted in violet color (Bracannot et al., 2012). For the PLIO results, the LGM ice cover is used, since the assumption of modern soil depth is heavily violated in these regions.

5. Discussion

In this section, we synthesize and interpret the global results of all the models, including scenarios with and without the penalty function in Model 3. For brevity, we limit our discussion of regional variations to Tibet, Europe and South America. For other regional areas of interest to readers, the data used in the following figures is available for download (see acknowledgements). Our presentation of selected regional areas is followed by the comparison of modeled FCI with published field observations. We also compare the model outcomes of all the three models used in the study. Finally, we discuss the study's limitations.

5.1. Synthesis and Interpretation

This section comprises the synthesis and interpretation of the global trends in FCI values predicted by Models 1-3 for the investigated paleoclimate simulations (PI, MH, LGM and PLIO). In all the paleoclimate simulations, high values of FCI in northern latitudes (60 °N – 80 °N) in Eurasia and North America coincide with lower MATs in the range of -25 °C to -5 °C and very high Ta's in the range of 30 °C to 40 °C. FCI in areas with negative MATs is mainly controlled by the Ta values, as higher Ta and high thermal gradients are predicted in the subsurface and

363 facilitate ice segregation growth (Hales and Roering, 2007; Hallet et al., 1991; Murton et al., 2006; Walder and
364 Hallet, 1985).

365 We also calculated the global sum of FCI for all paleoclimate time-slices to determine which Cenozoic timescale
366 is most important for frost cracking in each model. Furthermore, we compare the global sum of FCI in MH, LGM
367 and PLIO to that of PI simulations. Model 1 predicts a maximum FCI for the PI. These are 3.8%, 27%, and 25%
368 higher than the FCI values in the MH, LGM, and PLIO simulations, respectively. In Model 2, MH experiences
369 maximum FCI, which is 2.4% higher than in the PI, while FCIs in the LGM and PLIO simulations are 15% and
370 31% lower than in the PI. In Model 3 (scenario 1), the LGM and MH experience FCI values that are 22% and
371 12% higher than in the PI, while FCI in the PLIO is 30% lower than in the PI simulation. In Model 3 (scenario 2),
372 the MH experiences the maximum FCI, which is 3.5% higher than in the PI, while FCIs in LGM and PLIO
373 simulations are 21% and 29% lower than in the PI. The global sum of FCI estimates are consistent between Model
374 1, 2, and 3 (scenario 2) and suggest that maximum frost cracking (weathering) occurred during inter-glacial
375 periods (i.e. MH and PI), while the glacial period (LGM) experienced comparatively less frost cracking. The
376 above predictions for frost cracking (e.g. in Model 1, 2 and 3 (scenario 2)) are inconsistent with studies of global
377 weathering fluxes during glacial and inter-glacial periods, which reported an increase of weathering of ~20% in
378 the LGM (compared to the present) (Gibbs and Kump, 1994; Ludwig et al., 1999). This pattern is, however,
379 predicted by Model 3 (scenario 1) where the maximum in global frost cracking is predicted for the glacial period
380 (LGM). More specifically, Model 3 (scenario 1) predicts an FCI increase of 22% from PI values. This observation
381 is also consistent with the findings of a similar work by Marshall et al. (2015), who suggested that frost weathering
382 was higher during the LGM than today in unglaciated regions. These results highlight the importance of the
383 penalty function (i.e. dependency of FCI on distance to water) in first order (global) estimations of FCI.

384 ## 5.2. Influence of past climate on FCI on a global scale

385 We have investigated the influence of climate change on frost cracking on different spatial scales and through
386 geologic time using 3 different frost cracking models (Anderson, 1998; Hales and Roering 2007; Andersen et al.,
387 2015) and paleoclimate GCM simulations (Mutz et al., 2018). Our results for Model 3 are presented as maps
388 showing time-slice specific FCI anomalies relative to the PI climate simulation on a global scale (Fig. 8a, 9a, 10a),
389 in Europe (Fig. 8b, 9b, 10b), Tibet (Fig. 8c, 9c, 10c) and South America (Fig. 8d, 9d, 10d). Furthermore, we
390 highlighted where continental ice was located for all time-slices (PI, MH, LGM) or where Pleistocene ice cover
391 could result in a violation of our assumption of modern soil thickness (PLIO) (Fig. 8-10). This was done to prevent
392 unmerited regional comparisons of simulated FCI.

393 ### 5.2.1. Differences in FCI between PI and MH climate simulations

394 The differences in FCI between the PI and MH climate simulations are in the range of -0.04 °C m to 0.02 °C m
395 on a global scale (Fig. 8a). The MH simulation yields higher FCI values for most regions except for parts of
396 northern Asia, mid-western Europe, mid North America, the Andes Mountains and parts of Alaska and Tibet.
397 These differences may be attributed to the slight changes in MATs in these regions. The PI – MH comparisons
398 for Europe (Fig. 8b) reveal very small deviations in MH-FCI from PI conditions (ΔFCI $\approx$ -0.02 °C m to 0.02 °C
399 m). These changes are negative in Western Europe (including areas near the cities of Paris, Berlin and Rome),
400 and positive in Eastern Europe (including Budapest, Kiev and Moscow). Tibet exhibits only small (~0.02 *°C m*),

401   predominantly positive MH-FCI deviations from PI conditions (Fig. 8c). The magnitude of PI-MH FCI differences

402   in southwestern South America (Fig. 8d) is similar to that in other regions (ΔFCI ≈ -0.02 °C m to 0.02 °C m).

403
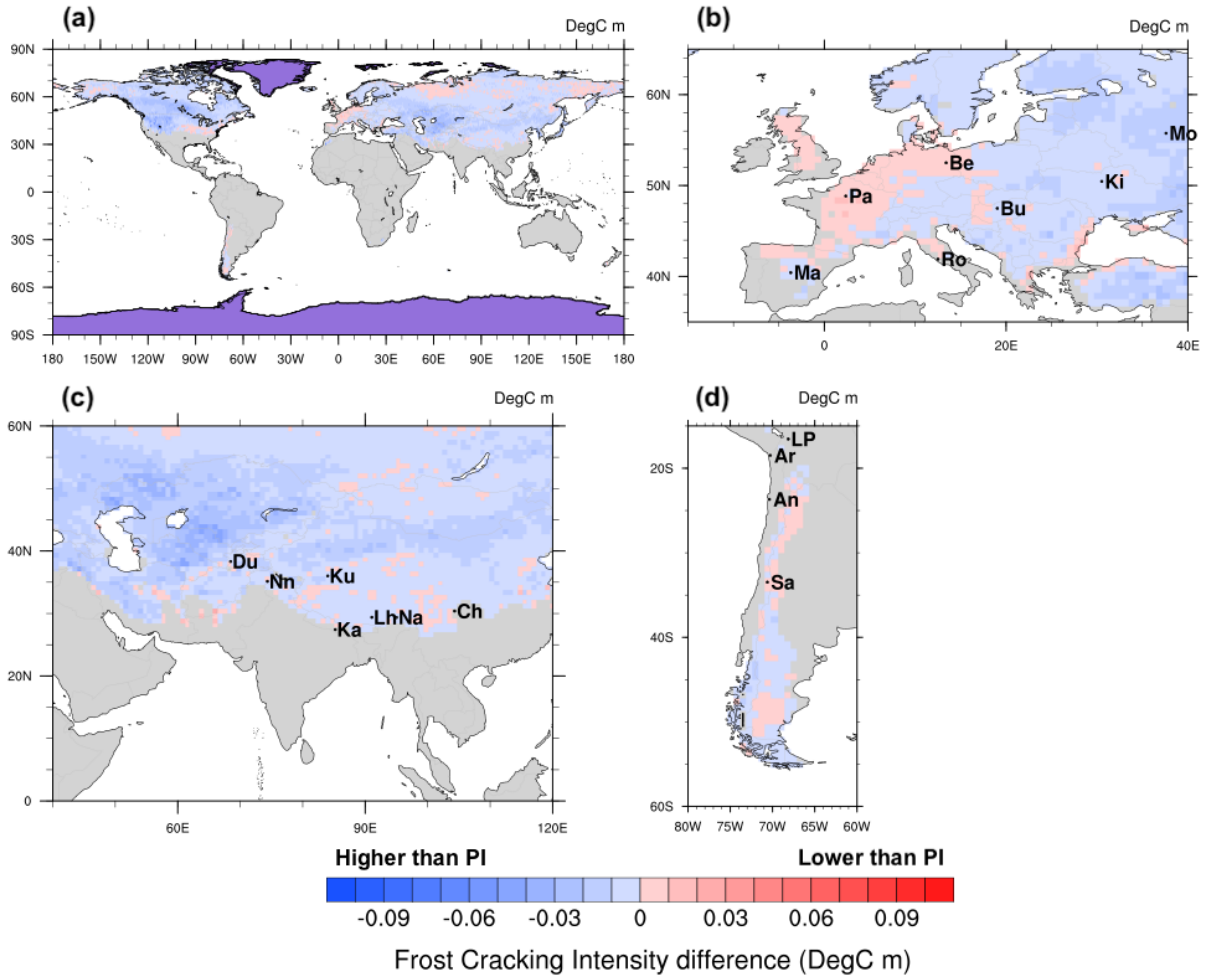
Figure 8. Differences between (Model 3) predictions of Pre-Industrial and Mid-Holocene long-term FCI means (unit: °C m) for (a) the entire Earth surface, (b) Europe, (c) South Asia, and (d) South America . Glacial cover is highlighted in violet. City abbreviations: Tibet:- Du – Dushambe, Nn – Srinagar, Ku – Xinjiang, Ka – Kathmandu, Lh – Lhasa, Na – Namcha Barwa, Ch – Chenshangou; Europe:- Pa – Paris, Be – Berlin, Mo – Moscow, Ki – Kiev, Ro – Rome, Bu – Budapest, Ma – Madrid; South America:- LP – La Paz, Ar – Arica, An – Antofagasta, Sa – Santiago. The regions covered by ice were removed from the calculation and are highlighted in violet color (Bracannot et al., 2012).

410   **5.2.2.   Differences in FCI between PI and LGM climate simulations**

411   The differences in FCI between PI and LGM on global scale (Fig. 9a) are highest in the mid-high latitudes (~42

412   °N) in North America (ΔFCI ≈ 0.08 °C m) and northern Asia (~75 °N) (ΔFCI ≈ 0.07 °C m). The close proximity

413   of these regions to the glacier cover in the LGM highlights the possibility of the presence of periglacial

414   environments that support frost cracking (Marshall et al., 2015) during the PI. This is also observed in the mid-

415   high latitudes in Asia (30 °N – 50 °N) (ΔFCI ≈ 0.04 °C m), which may be attributed to the positive MATs in this

416   region during the PI simulation.
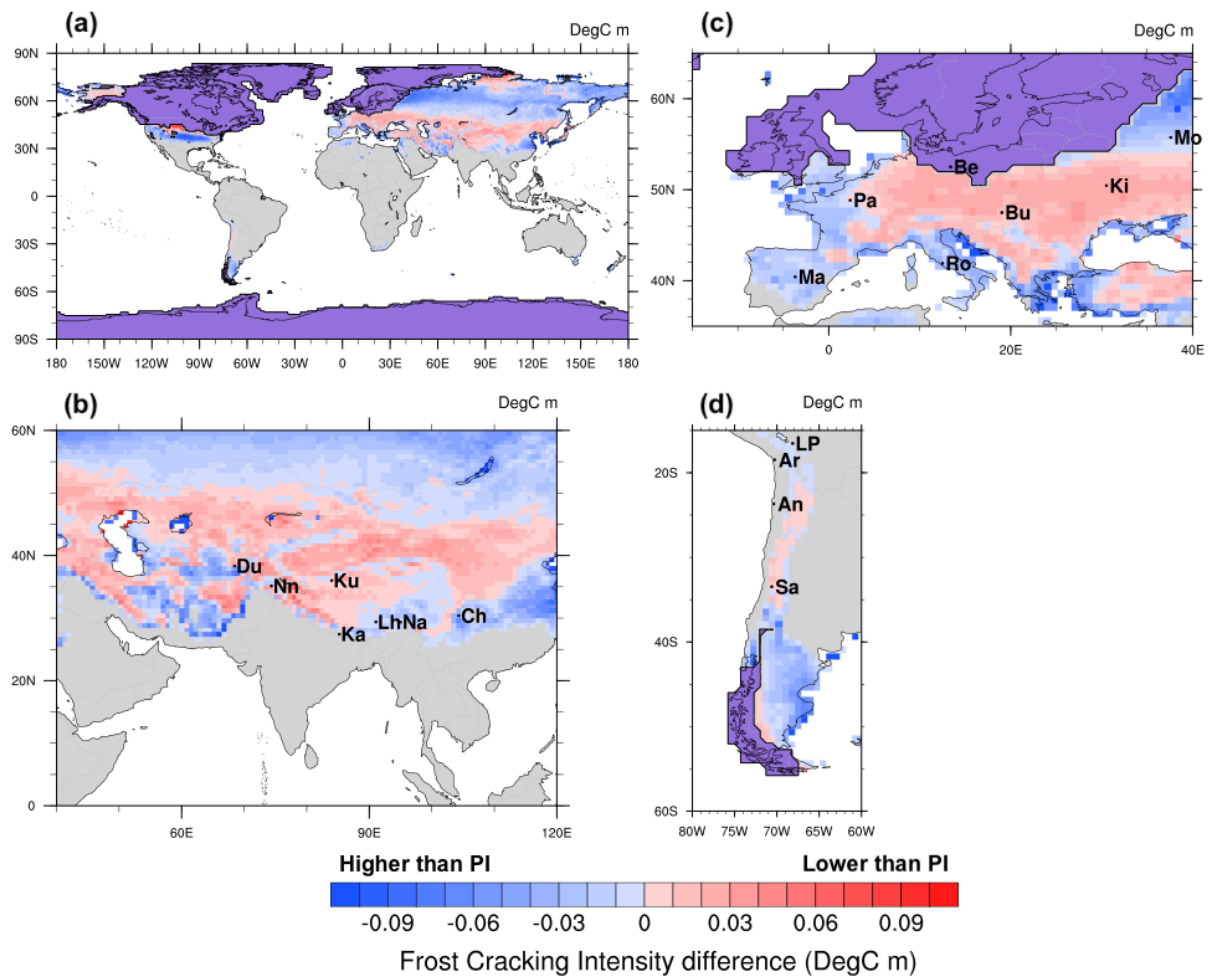
Figure 9. Differences between (Model 3) predictions of Pre-Industrial and Last Glacial Maximum long-term FCI means (unit: °C m) for (a) the entire Earth surface, (b) Europe, (c) South Asia, and (d) South America. Glacial cover is highlighted in violet. City abbreviations: Tibet:- Du – Dushambe, Nn – Srinagar, Ku – Xinjiang, Ka – Kathmandu, Lh – Lhasa, Na – Namcha Barwa, Ch – Chenshangou; Europe:- Pa – Paris, Be – Berlin, Mo – Moscow, Ki – Kiev, Ro – Rome, Bu – Budapest, Ma – Madrid; South America:- LP – La Paz, Ar – Arica, An – Antofagasta, Sa – Santiago. The regions covered by ice were removed from the calculation and are highlighted in violet color (Bracannot et al., 2012).

However, in the higher latitudes of Asia (~ 50 °N to 70 °N) and South America (~ 40 °S to 50 °S), the LGM experiences more frost cracking than the PI (ΔFCI ≈ - 0.03 - -0.06 °C m). This can be attributed to higher Ta values (Fig. 3) in these regions during the LGM. In central Europe (Fig. 9b), including Paris, Budapest and Kiev, the PI shows higher FCI (ΔFCI ≈ 0.02 – 0.06 °C m) than the LGM. On the other hand, the LGM simulations predict higher FCI (ΔFCI ≈ -0.02 - -0.06 °C m) in southern Europe (including Madrid and Rome). Overall, the Tibetan Plateau experiences higher FCI values (ΔFCI ≈ 0.06 °C m) during the PI (Fig. 9c). Only in the eastern part of Tibet, near Lhasa, LGM FCI values are higher (ΔFCI ≈ 0.04 °C m). In South America (Fig. 9d), the LGM yields lower FCI values (ΔFCI ≤ 0.06 °C m) in the Andes Mountains, and the PI simulation yields lower FCI values (ΔFCI≥ -0.06 °C m) in the east of the Andes Mountains in the southern part of the region (40 °S – 50 °S).

5.2.3. Differences in FCI between PI and PLIO climate simulations

18
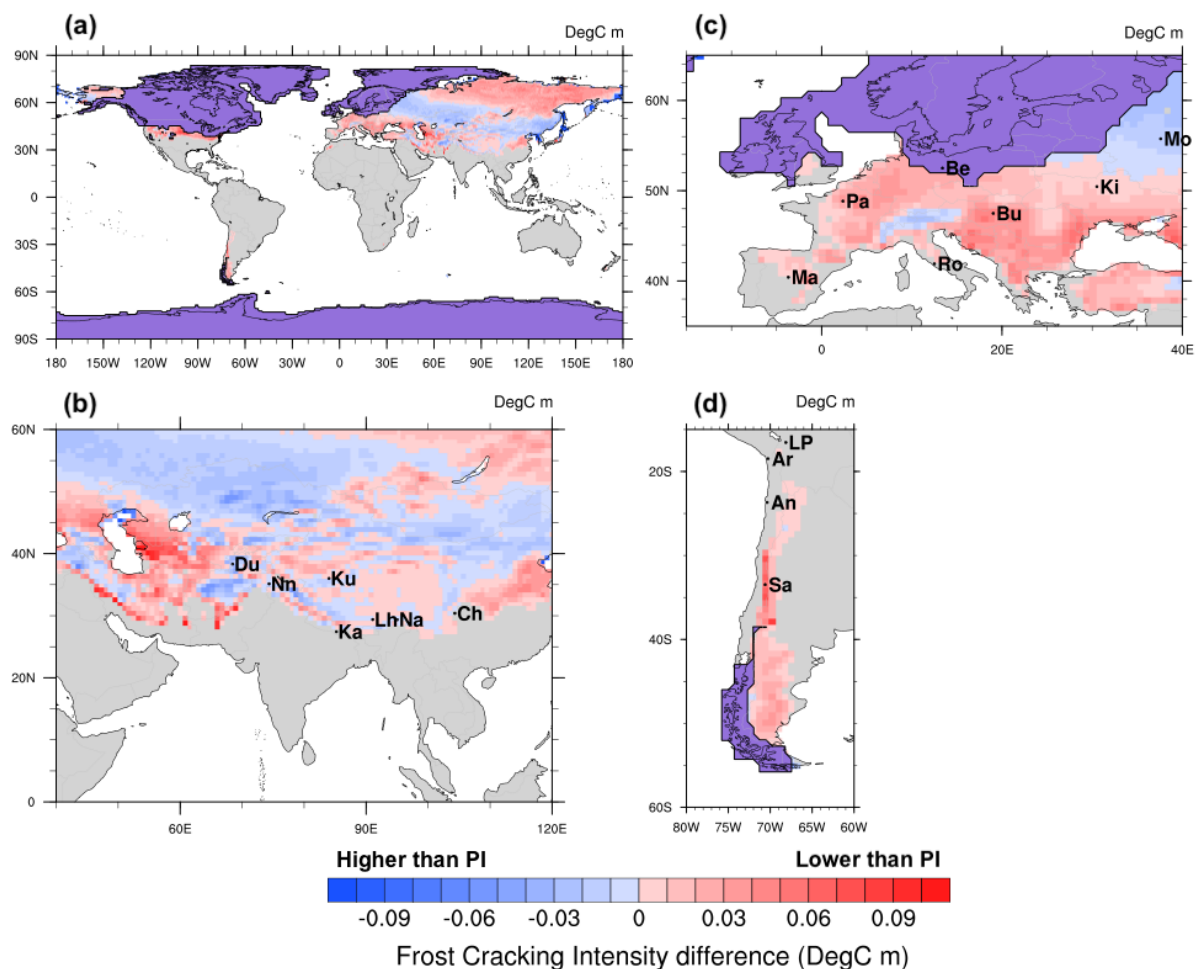
Figure 10. Differences between (Model 3) predictions of Pre-Industrial and Pliocene long-term FCI means (unit: °C m) for (a) the entire Earth surface, (b) Europe, (c) South Asia, and (d) South America. Maximum Pleistocene glacial cover is highlighted in violet. City abbreviations: Tibet:- Du – Dushambe, Nn – Srinagar, Ku – Xinjiang, Ka – Kathmandu, Lh – Lhasa, Na – Namcha Barwa, Ch – Chenshangou; Europe:- Pa – Paris, Be – Berlin, Mo – Moscow, Ki – Kiev, Ro – Rome, Bu – Budapest, Ma – Madrid; South America:- LP – La Paz, Ar – Arica, An – Antofagasta, Sa – Santiago. The regions covered by ice were removed from the calculation and are highlighted in violet color (Bracannot et al., 2012).

Frost cracking is higher in the PI than in the PLIO (Fig. 10a) (ΔFCI $\approx$ 0.04 – 0.08 °C m) in the mid-to-high latitudes of Europe and North America (35 °N – 55 °N), and in higher latitudes in Asia (50 °N – 80 °N). This can be attributed to the warmer climate during PLIO and high Ta (Fig. 3) in the PI simulation. However, the PLIO exhibits marginally higher frost cracking in some regions of Asia and Alaska, where MATs are in the range of 0 – 5 °C.

In central to southern Europe, including Madrid, Paris, Rome, Budapest and Kiev, PI-FCI values are moderate (ΔFCI $\approx$ 0.02 °C m - 0.06 °C m). On the Tibetan Plateau (Fig. 10c), PI-FCI values are higher (ΔFCI $\approx$ 0.04 °C m) over most of the region, except for the eastern slopes of Himalayas, where PLIO-FCI values are higher than European region (ΔFCI $\approx$ -0.04 °C m). South America experienced largest differences in FCI (ΔFCI $\approx$ 0.02 °C m to 0.08 °C m) (Fig. 10d). This is likely caused by high temperatures in the Pliocene (Mutz et al., 2018), which prevented the bedrock in the mid-latitude regions of South America to reach the FCW.

In summary, the comparison of differences between paleo-FCI and PI-FCI indicate a low impact of changing

19

surface temperatures between the PI and MH simulations on frost cracking. This is not surprising given the relatively small climatological differences between the simulations. The differences in FCI between the PLIO and PI are more varied, but generally greater. The LGM simulation produced the greatest differences in FCI with respect to the PI simulation. These differences can be attributed to increased glaciation and a much colder climate in higher latitudes, including North America and Europe. High LGM-FCI values were exhibited east of the Andes Mountains in the southern part of South America, possibly due to lower MATs (Fig. 2) and high Ta values (~ 20 °C – 25 °C) (Fig. 3) during the LGM. The above interpretations are in agreement with Mutz et al. (2018) and Mutz and Ehlers (2019) who suggested minor deviation of MH MATs from PI values for these regions, and higher deviations in the LGM and PLIO simulations.

5.3.   Comparison to previous related studies

In this section, we discuss the broad trends of modeled FCI in the context of variations in MAT, Ta, and water availability. We do this to document how these changes compare to findings of previous studies. We found that FCI and Ta are highly (and significantly) correlated in our models. For example, Model 3 (scenario 1) results yield significant Pearson r values in the range of $0.8 - 0.9$. This is consistent with findings by Rempel et al. (2016), who suggested that for the same MAT and rock properties, FCI is expected to be higher for regions with higher Ta, as steeper temperature gradients supports more liquid transport. Walder and Hallet (1985) suggested that FCI is higher for moderately low, negative MATs and that frost cracking in cold regions could persist due to water transport in cold bedrock. The assumption of positive temperatures (and availability of liquid water) at either boundary (i.e. at surface and 20 m depth) in Models 1, 2 and 3 is inconsistent with above statement. The inclusion of a penalty function, which represents the dependency of FCI on distance to water, leads to higher global sums of FCI during colder climates. More specifically, the inclusion of the penalty function predicts LGM-FCI values to be 20% higher than in the PI. This is in line with studies of global chemical weathering fluxes (Gibbs and Kump, 1994; Ludwig et al., 1999). Finally, recent work (Marshall et al., 2015a, 2017) for Western Oregon, USA, suggested that periglacial processes were vigorous during the LGM, which is supported by our model showing increased FCI values in the LGM (see Fig. 9a) for periglacial regions (42 °N – 44 °N; 115 °W – 125 °W) in North America. Taken together, previous studies are consistent with the broad trends in FCI predicted by our global analysis.

5.4.   Inter-comparison of Models 1-3

A comparison of the FCI predicted by the three models for the different time slices highlights some key differences (Fig. 6, and supplement Figs. 1, 2). The pattern of global sums in FCI values in specific time-slices is different in all the three models, which can be accredited to different inputs considered in each model. These inputs include the availability of water for frost cracking by segregation ice growth, and the volume of available water (with and without consideration of distance to water). For example, Model 1, Model 2, Model 3 (scenario 1: with penalty function), and Model 3 (scenario 2: without penalty function) predict the global sum of FCI to be greatest in the PI, MH, LGM and MH, respectively.

Model 1 predicts the maximum FCI values in the regions with MATs in the range of -10 °C to -5 °C, relatively low FCI values in regions with MATs of -5 °C – 0 °C, and very low values in regions characterized by high MATs above 0 °C. In contrast, Model 2 (Supplement Fig. 2) and Model 3 yield maximum FCI values for positive MATs with high Ta, as observed in previous studies (Andersen et al., 2015; Anderson et al., 2013; Hales and Roering,

494   2007; Marshall et al., 2015). In Model 3, the soil thickness plays an important role in the estimation of the FCI.

495   The model predicts high FCI values for areas with low soil thickness, such as < 5 cm in Eurasia (55 °E – 80 °E,

496   35 °N – 50 °N) and 10 cm to 20 cm for North America (50 °N – 63 °N; 70 °N – 80 °N). This result is in close

497   agreement with Andersen et al. (2015). Due to the lower penetration depths of the freezing front, the FCI is

498   considerably dampened in the presence of the soil cover, thereby limiting the bedrock from reaching FCW in

499   cases of positive MATs (Andersen et al., 2015).

500   The spatial pattern of frost cracking in Model 3 is influenced by consideration of segregation ice growth, in which

501   the available volume of water (V_W) in the vicinity of an ice lens is critical. Segregation ice growth and sediment

502   cover are responsible for the observed patterns in FCI. The other models considered (see supplement Fig. 1, 2)

503   do not explicitly account for both these processes and therefore produce different predictions of the FCI in some

504   regions.

505

506   **5.5.   Model Limitations**

507   Here we discuss the limitations of the 3 frost cracking models and uncertainties stemming from the application of

508   the ECHAM5 simulations as input to these models. One of the most important limitations in this study is the use

509   of the same soil thickness for each of our paleoclimate time-slices (Wieder, 2014). In reality, the soil thickness

510   may be different for PI, MH, LGM, and PLIO due to erosion and sedimentation, and temporal variations in soil

511   production. However, there are currently no other global estimates of paleo soil thickness available. Therefore,

512   using present-day thickness remains the best-informed and feasible approach. Nevertheless, we stress that our

513   modelled FCI values should be regarded as the predicted FCI response to climate change without consideration

514   of weathering – soil thickness dynamics. Furthermore, uniform thermal diffusivity and porosity were used for

515   bedrock and sediment cover over the globe for simplification, even though thermal diffusivity and porosity vary

516   for different Earth materials. The application of different thermal diffusivities for individual lithologies was not

517   considered, although typical thermoconductivity variations of rocks can vary by a factor of 2-3 at the most (Ehlers,

518   2005). In addition, our models neglect the hydrogeological properties of bedrock, including moisture content and

519   permeability for the calculation of subsurface temperature variations, which may influence water availability for

520   frost cracking. To the best of our knowledge, there are no global inventories of these properties that are suited for

521   studies such as ours. In our approach, we assume that these material properties are spatially and temporally

522   constant. As a result, our predictions are only suited as adequate representations of regional trends in FCI, and the

523   reader is advised that local deviations from our values are likely and will depend on near surface geologic and

524   hydrologic variations. Although the GCM simulations presented are at a high-resolution (from the perspective of

525   the climate modeling community) they are nevertheless coarse from the perspective of local geomorphic

526   processes. The coarse spatial resolution of our models raises several issues for more detailed geomorphic analyses.

527   More specifically, in regions with bare bedrock, the model assumes the presence of a soil layer with 30% porosity,

528   which compromises our model results. Furthermore, the coarse spatial resolutions of the paleoclimate simulations

529   (a ~ 80 x 80 km horizontal grid) and low soil thickness spatial resolution (5 km) complicates the consideration of

530   subgrid variations in regions characterised by complex and high topography (e.g. European Alps, Himalayas or

531   Andes). For future studies in such terrain, this problem may be addressed by regional climate downscaling (e.g.

532   Fiddes and Gruber, 2014 and Wang et al., 2021) and the use of high resolution lithologic, and soil distribution

533   data (when available). A further source of uncertainties stems from possible inaccuracies in paleoclimate estimates

534   that drive the frost cracking models. The reader is referred to Mutz et al. (2018) for further discussion of the

535   GCM's limitations. Given the above limitations, we cautiously highlight that the results presented here are

536   essentially maps of FCI sensitivity to climate change forcing. Although broad agreement is found between our

537   predictions and previous work (Section 5.5), we caution that geologic and hydrologic complexities in the 'real

538   world' may produce variations in FCI driven by hydrologic and geologic heterogeneities we are unable to account

539   for.

540   Finally, it is worth noting that only selected time slices were evaluated here. Although the LGM was a significant

541   global glacial event, previous (and more extreme) ice ages occurred in the Quaternary. Therefore, the spatial

542   patterns of FCI predicted here may not match observations in all areas, particularly where they have a 'periglacial

543   hangover' of frost cracking from previous glaciations.

6. Conclusions

545   We presented three approaches to quantify the frost cracking intensity (FCI) for different times in the Late

546   Cenozoic, namely pre-industrial (PI, ~1850 CE), Mid-Holocene (MH, ~6 ka), Las Glacial Maximum (LGM, ~21

547   ka) and mid-Pliocene (PLIO, ~3 Ma). These approaches are based on process-informed frost cracking models and

548   their coupling to paleoclimate simulations (Mutz et al., 2018). A simple one-dimensional heat conduction model

549   (Hales and Roering, 2007) was applied along with FCI estimation approaches from Anderson (1998) and

550   Andersen et al. (2015). Our analysis and presentation of results focused on the most recent and more thoroughly

551   parameterized approach of Andersen et al., (2015; Model 3). Specifically, we quantified the change in direction

552   and magnitude of FCI in the above-mentioned climate states with respect to the PI control simulation. The major

553   findings of our study include:

554   1.   The latitudinal extent of frost cracking in the PI and MH are very similar, in Eurasia (28 °N – 80 °N),

555   North America (40 °N – 80 °N) and South America (20 °S – 55 °S). During the LGM, the FCI extent is

556   reduced in Eurasia (28 °N – 78 °N) and North America (35 °N – 75 °N), and increased in South America

557   (15 °S – 55 °S). This can be attributed to extensive glaciation in the northern parts of Canada, Greenland

558   and Northern Europe not favoring the frost cracking process due to more persistently cold conditions in

559   these regions. In the PLIO, the FCI extent is similar to that of PI in Eurasia (30 °N – 80 °N) and North

560   America (40 °N – 85 °N). PLIO-FCI values are higher in Canada (~ 0.16 $°C\,m$ to 0.18 $°C\,m$) and

561   Greenland (~ 0.08 $°C\,m$), but significantly reduced in South America (21 °S – 55 °S) with values of FCI

562   below 0.02 $°C\,m$.

563   2.   MH climatic conditions induce only small deviations of FCI from PI values, whereas the colder (LGM)

564   and warmer (PLIO) climates produce larger FCI anomalies, which are consistent with the findings of

565   Mutz and Ehlers, (2019).

566   3.   Global sums of the FCI predicted by Model 3 - scenario 1, which is based on Andersen et al., (2015)

567   which makes FCI dependent on distance to water, are highest for the LGM. Our models predict a global

568   FCI increase of 22% (relative to PI) in non-glaciated regions for this time period.

569   The predicted changes in FCI presented here do not entirely confirm our hypothesis that: Late Cenozoic global

570   climate change resulted in varying intensity in FCI such that more intense frost cracking occurs at lower latitudes

571   during colder climates. Of particular interest is that although we document latitudinally influenced spatial and

572 temporal changes in FCI, these changes are not uniform at the same latitude. The largest changes in FCI between
573 time slices occur in different geographic regions at different time periods meaning that a more simplified approach
574 of assuming only latitudinal shifts in FCI between cold and warm periods is not sufficient and that spatial changes
575 in global climate need to be considered.

576 Finally, we suggest that Model 3 can be adapted in future work to regional conditions, using field geological and
577 hydrogeological parameters for better accuracy (Andersen et al., 2015). The results of this study can further be
578 used in modelling the erosion and denudation processes related to frost cracking, or for the interpretation of
579 catchment average erosion rates from cosmogenic radionuclide data. Predictions for potential future sites that are
580 prone to hazards related to frost cracking, such as rockfall, can be generated by coupling these models to climate
581 simulations forced with different greenhouse gas concentration scenarios representing different possible climate
582 conditions of the future.

583 **Code availability**

584 The code and data used in this study are freely available upon request.

585 **Author contributions**

586 HS, SM and TAE designed the initial model setup and simulation programs and conducted model modifications,
587 simulation runs and analysis. HS and TAE prepared the manuscript with contributions from SM.

588 **Competing interests**

589 The authors declare that they have no competing interests.

599 **References**

600 Abe-Ouchi, A., Saito, F., Kageyama, M., Braconnot, P., Harrison, S. P., Lambeck, K., Otto-Bliesner, B. L., Peltier,
601 W. R., Tarasov, L., Peterschmitt, J.-Y., and Takahashi, K.: Ice-sheet configuration in the CMIP5/PMIP3 Last
602 Glacial Maximum experiments, Geosci. Model Dev., 8, 3621–3637, https://doi.org/10.5194/gmd-8-3621-2015,
603 2015.

604 Acosta, V. T., Schildgen, T. F., Clarke, B. A., Scherler, D., Bookhagen, B., Wittmann, H., von Blanckenburg, F.,

605 and Strecker, M. R.: Effect of vegetation cover on millennial-scale landscape denudation rates in East Africa, 7,

606 408–420, https://doi.org/10.1130/l402.1, 2015.

607 Adams, B. A., Whipple, K. X., Forte, A. M., Heimsath, A. M., and Hodges, K. V.: Climate controls on erosion in

608 tectonically active landscapes, Sci. Adv., 6, eaaz3166, https://doi.org/10.1126/sciadv.aaz3166, 2020.

609 Amitrano, D., Gruber, S., and Girard, L.: Evidence of frost-cracking inferred from acoustic emissions in a high-

610 alpine rock-wall, Earth and Planetary Science Letters, 341–344, 86–93,

611 https://doi.org/10.1016/j.epsl.2012.06.014, 2012.

612 Andersen, J. L., Egholm, D. L., Knudsen, M. F., Jansen, J. D., and Nielsen, S. B.: The periglacial engine of

613 mountain erosion - Part 1: Rates of frost cracking and frost creep, Earth Surf. Dynam., 3, 447–462,

614 https://doi.org/10.5194/esurf-3-447-2015, 2015.

615 Anderson, R. S.: Near-surface Thermal Profiles in Alpine Bedrock: Implications for the Frost Weathering of Rock,

616 Arctic and Alpine Research, 30, 362–372, https://doi.org/10.1080/00040851.1998.12002911, 1998.

617 Anderson, R. S., Anderson, S. P., and Tucker, G. E.: Rock damage and regolith transport by frost: an example of

618 climate modulation of the geomorphology of the critical zone: ROCK DAMAGE AND REGOLITH

619 TRANSPORT BY FROST, Earth Surf. Process. Landforms, 38, 299–316, https://doi.org/10.1002/esp.3330, 2013.

620 Arnold, L., Bréon, F.-M., and Brewer, S.: The Earth as an extrasolar planet: the vegetation spectral signature today

621 and during the last Quaternary climatic extrema, International Journal of Astrobiology, 8, 81–94,

622 https://doi.org/10.1017/S1473550409004406, 2009.

623 Bigelow, N. H., Brubaker, L. B., Edwards, M. E., Harrison, S. P., Prentice, I. C., Anderson, P. M., Andreev, A.

624 A., Bartlein, P. J., Christensen, T. R., Cramer, W., Kaplan, J. O., Lozhkin, A. V., Matveyeva, N. V., Murray, D.

625 F., McGuire, A. D., Razzhivin, V. Y., Ritchie, J. C., Smith, B., Walker, D. A., Gajewski, K., Wolf, V., Holmqvist,

626 B. H., Igarashi, Y., Kremenetskii, K., Paus, A., Pisaric, M. F. J., and Volkova, V. S.: Climate change and Arctic

627 ecosystems: 1. Vegetation changes north of 55°N between the last glacial maximum, mid-Holocene, and present,

628 108, https://doi.org/10.1029/2002JD002558, 2003.

629 Botsyun, S., Ehlers, T. A., Mutz, S. G., Methner, K., Krsnik, E., and Mulch, A.: Opportunities and Challenges for

630 Paleoaltimetry in "Small" Orogens: Insights From the European Alps, Geophysical Research Letters, 47,

631 e2019GL086046, https://doi.org/10.1029/2019GL086046, 2020.

632 Braconnot, P., Harrison, S., Kageyama, M. *et al.* Evaluation of climate models using palaeoclimatic data. *Nature*

633 *Clim Change* **2,** 417–424 (2012). https://doi.org/10.1038/nclimate1456

634 Davidson, G. P. and Nye, J. F.: A photoelastic study of ice pressure in rock cracks, Cold Regions Science and

635 Technology, 11, 141–153, https://doi.org/10.1016/0165-232X(85)90013-8, 1985.

636 Delunel, R., van der Beek, P. A., Carcaillet, J., Bourlès, D. L., and Valla, P. G.: Frost-cracking control on

637 catchment denudation rates: Insights from in situ produced 10Be concentrations in stream sediments (Ecrins–

638 Pelvoux massif, French Western Alps), Earth and Planetary Science Letters, 293, 72–83,
639 https://doi.org/10.1016/j.epsl.2010.02.020, 2010.

640 Dietrich, S., Werner, M., Spangehl, T., and Lohmann, G.: Influence of orbital forcing and solar activity on water
641 isotopes in precipitation during the mid - and late Holocene, 9, 13–26, https://doi.org/10.5194/cp-9-13-2013, 2013.

642 Dowsett, H., Robinson, M., Haywood, A., Salzmann, U., Hill, D., Sohl, L., Chandler, M., Williams, M., Foley,
643 K., and Stoll, D.: The PRISM3D paleoenvironmental reconstruction, Stratigraphy, 7, 123–139, 2010.

644 Draebing, D., Haberkorn, A., Krautblatter, M., Kenner, R., and Phillips, M.: Thermal and Mechanical Responses
645 Resulting From Spatial and Temporal Snow Cover Variability in Permafrost Rock Slopes, Steintaelli, Swiss Alps:
646 Thermal and Mechanical Responses to Snow in Permafrost Rock Slopes, Permafrost and Periglac. Process., 28,
647 140–157, https://doi.org/10.1002/ppp.1921, 2017.

648 Ehlers, T. A. and Poulsen, C. J.: Influence of Andean uplift on climate and paleoaltimetry estimates, Earth and
649 Planetary Science Letters, 281, 238–248, https://doi.org/10.1016/j.epsl.2009.02.026, 2009.

650 Eppelbaum, T. A., Kutasov, I., and Pilchin, A.: Thermal Properties of Rocks and Density of Fluids, in: Applied
651 Geothermics, Springer-Verlag Berlin Heidelberg, 99–149, 2014.

652 Eppes, M.-C. and Keanini, R.: Mechanical weathering and rock erosion by climate-dependent subcritical cracking:
653 WEATHERING BY SUBCRITICAL CRACKING, Rev. Geophys., 55, 470–508,
654 https://doi.org/10.1002/2017RG000557, 2017.

655 Etheridge, D. M., Steele, L. P., Langenfelds, R. L., Francey, R. J., Barnola, J.-M., and Morgan, V. I.: Natural and
656 anthropogenic changes in atmospheric CO_2 over the last 1000 years from air in Antarctic ice and firn, Journal of
657 Geophysical Research: Atmospheres, 101, 4115–4128, https://doi.org/10.1029/95JD03410, 1996.

658 Etheridge, D. M., Steele, L. P., Francey, R. J., and Langenfelds, R. L.: Atmospheric methane between 1000 A.D.
659 and present: Evidence of anthropogenic emissions and climatic variability, Journal of Geophysical Research:
660 Atmospheres, 103, 15979–15993, https://doi.org/10.1029/98JD00923, 1998.

661 Fiddes, J. and Gruber, S.: TopoSCALE v.1.0: downscaling gridded climate data in complex terrain, Geosci. Model
662 Dev., 7, 387–405, https://doi.org/10.5194/gmd-7-387-2014, 2014.

663 Gibbs, M. T. and Kump, L. R.: Global chemical erosion during the Last Glacial Maximum and the present:
664 Sensitivity to changes in lithology and hydrology, Paleoceanography, 9, 529–543,
665 https://doi.org/10.1029/94PA01009, 1994.

666 Girard, L., Gruber, S., Weber, S., and Beutel, J.: Environmental controls of frost cracking revealed through in situ
667 acoustic emission measurements in steep bedrock: IN SITU MEASUREMENTS OF FROST CRACKING,
668 Geophys. Res. Lett., 40, 1748–1753, https://doi.org/10.1002/grl.50384, 2013.

669 Hales, T. C. and Roering, J. J.: Climatic controls on frost cracking and implications for the evolution of bedrock
670 landscapes, J. Geophys. Res., 112, F02033, https://doi.org/10.1029/2006JF000616, 2007.

671   Hales, T. C. and Roering, J. J.: A frost "buzzsaw" mechanism for erosion of the eastern Southern Alps, New

672   Zealand, Geomorphology, 107, 241–253, https://doi.org/10.1016/j.geomorph.2008.12.012, 2009.

673   Hallet, B., Walder, J. S., and Stubbs, C. W.: Weathering by segregation ice growth in microcracks at sustained

674   subzero temperatures: Verification from an experimental study using acoustic emissions, Permafrost Periglac.

675   Process., 2, 283–300, https://doi.org/10.1002/ppp.3430020404, 1991.

676   Harrison, S. P., Yu, G., Takahara, H., and Prentice, I. C.: Diversity of temperate plants in east Asia, Nature, 413,

677   129–130, https://doi.org/10.1038/35093166, 2001.

678   Hasler, A., Gruber, S., and Haeberli, W.: Temperature variability and offset in steep alpine rock and ice faces,

679   The Cryosphere, 5, 977–988, https://doi.org/10.5194/tc-5-977-2011, 2011.

680   Haywood, A. M., Dowsett, H. J., Otto-Bliesner, B., Chandler, M. A., Dolan, A. M., Hill, D. J., Lunt, D. J.,

681   Robinson, M. M., Rosenbloom, N., Salzmann, U., and Sohl, L. E.: Pliocene Model Intercomparison Project

682   (PlioMIP): experimental design and boundary conditions (Experiment 1), Geosci. Model Dev., 3, 227–242,

683   https://doi.org/10.5194/gmd-3-227-2010, 2010.

684   Herman, F. and Champagnac, J.-D.: Plio-Pleistocene increase of erosion rates in mountain belts in response to

685   climate change, Terra Nova, 28, 2–10, https://doi.org/10.1111/ter.12186, 2016.

686   Herman, F., Seward, D., Valla, P. G., Carter, A., Kohn, B., Willett, S. D., and Ehlers, T. A.: Worldwide

687   acceleration of mountain erosion under a cooling climate, Nature, 504, 423–426,

688   https://doi.org/10.1038/nature12877, 2013.

689   Kellerer-Pirklbauer, A.: Potential weathering by freeze-thaw action in alpine rocks in the European Alps during a

690   nine year monitoring period, Geomorphology, 296, 113–131, https://doi.org/10.1016/j.geomorph.2017.08.020,

691   2017.

692   Lease, R. O. and Ehlers, T. A.: Incision into the Eastern Andean Plateau During Pliocene Cooling, Science, 341,

693   774–776, https://doi.org/10.1126/science.1239132, 2013.

694   Lohmann, G., Pfeiffer, M., Laepple, T., Leduc, G., and Kim, J.-H.: A model-data comparison of the Holocene

695   global sea surface temperature evolution, 9, 1807–1839, https://doi.org/10.5194/cp-9-1807-2013, 2013.

696   Lorenz, S. J. and Lohmann, G.: Acceleration technique for Milankovitch type forcing in a coupled atmosphere-

697   ocean circulation model: method and application for the Holocene, Climate Dynamics, 23, 727–743,

698   https://doi.org/10.1007/s00382-004-0469-y, 2004.

699   Ludwig, W., Amiotte-Suchet, P., and Probst, J.: Enhanced chemical weathering of rocks during the last glacial

700   maximum: a sink for atmospheric CO_2?, Chemical Geology, 159, 147–161, https://doi.org/10.1016/S0009-

701   2541(99)00038-8, 1999.

702   Marshall, J. A., Roering, J. J., Bartlein, P. J., Gavin, D. G., Granger, D. E., Rempel, A. W., Praskievicz, S. J., and

703   Hales, T. C.: Frost for the trees: Did climate increase erosion in unglaciated landscapes during the late

704   Pleistocene?, Sci. Adv., 1, e1500715, https://doi.org/10.1126/sciadv.1500715, 2015.

705 Marshall, J. A., Roering, J. J., Gavin, D. G., and Granger, D. E.: Late Quaternary climatic controls on erosion
706 rates and geomorphic processes in western Oregon, USA, Geological Society of America Bulletin, 129, 715–731,
707 https://doi.org/10.1130/B31509.1, 2017.

708 Matsuoka, N.: Direct observation of frost wedging in alpine bedrock, Earth Surf. Process. Landforms, 26, 601–
709 614, https://doi.org/10.1002/esp.208, 2001.

710 Matsuoka, N.: Frost weathering and rockwall erosion in the southeastern Swiss Alps: Long-term (1994–2006)
711 observations, Geomorphology, 99, 353–368, https://doi.org/10.1016/j.geomorph.2007.11.013, 2008.

712 Messenzehl, K., Meyer, H., Otto, J.-C., Hoffmann, T., and Dikau, R.: Regional-scale controls on the spatial
713 activity of rockfalls (Turtmann Valley, Swiss Alps) — A multivariate modeling approach, Geomorphology, 287,
714 29–45, https://doi.org/10.1016/j.geomorph.2016.01.008, 2017.

715 Murton, J. B., Peterson, R., and Ozouf, J.-C.: Bedrock Fracture by Ice Segregation in Cold Regions, Science, 314,
716 1127–1129, https://doi.org/10.1126/science.1132127, 2006.

717 Mutz, S. G. and Ehlers, T. A.: Detection and explanation of spatiotemporal patterns in Late Cenozoic
718 palaeoclimate change relevant to Earth surface processes, Earth Surf. Dynam., 7, 663–679,
719 https://doi.org/10.5194/esurf-7-663-2019, 2019.

720 Mutz, S. G., Ehlers, T. A., Werner, M., Lohmann, G., Stepanek, C., and Li, J.: Estimates of late Cenozoic climate
721 change relevant to Earth surface processes in tectonically active orogens, Earth Surf. Dynam., 6, 271–301,
722 https://doi.org/10.5194/esurf-6-271-2018, 2018.

723 Otto-Bliesner, B. L., Brady, E. C., Clauzet, G., Tomas, R., Levis, S., and Kothavala, Z.: Last Glacial Maximum
724 and Holocene Climate in CCSM3, J. Climate, 19, 2526–2544, https://doi.org/10.1175/JCLI3748.1, 2006.

725 Peizhen, Z., Molnar, P., and Downs, W. R.: Increased sedimentation rates and grain sizes 2±4 Myr ago due to the
726 in¯uence of climate change on erosion rates, 410, 7, 2001.

727 Perron, J. T.: Climate and the Pace of Erosional Landscape Evolution, 45, 561–591,
728 https://doi.org/10.1146/annurev-earth-060614-105405, 2017.

729 Pickett, E. J., Harrison, S. P., Hope, G., Harle, K., Dodson, J. R., Peter Kershaw, A., Colin Prentice, I., Backhouse,
730 J., Colhoun, E. A., D'Costa, D., Flenley, J., Grindrod, J., Haberle, S., Hassell, C., Kenyon, C., Macphail, M.,
731 Martin, H., Martin, A. H., McKenzie, M., Newsome, J. C., Penny, D., Powell, J., Ian Raine, J., Southern, W.,
732 Stevenson, J., Sutra, J.-P., Thomas, I., Kaars, S., and Ward, J.: Pollen-based reconstructions of biome distributions
733 for Australia, Southeast Asia and the Pacific (SEAPAC region) at 0, 6000 and 18,000 14C yr BP: Palaeovegetation
734 patterns for Australia and Southeast Asia, 31, 1381–1444, https://doi.org/10.1111/j.1365-2699.2004.01001.x,
735 2004.

736 Prentice, I. C., Jolly, D., and BIOME 6000 Participants: Mid-Holocene and glacial-maximum vegetation
737 geography of the northern continents and Africa, J Biogeography, 27, 507–519, https://doi.org/10.1046/j.1365-
738 2699.2000.00425.x, 2000.

739   Rangwala, I. and Miller, J. R.: Climate change in mountains: a review of elevation-dependent warming and its
740   possible causes, Climatic Change, 114, 527–547, https://doi.org/10.1007/s10584-012-0419-3, 2012.

741   Raymo, M. E. and Ruddiman, W. F.: Tectonic forcing of late Cenozoic climate, Nature, 359, 117–122,
742   https://doi.org/10.1038/359117a0, 1992.

743   Rempel, A. W., Marshall, J. A., and Roering, J. J.: Modeling relative frost weathering rates at geomorphic scales,
744   Earth and Planetary Science Letters, 453, 87–95, https://doi.org/10.1016/j.epsl.2016.08.019, 2016.

745   Rode, M., Schnepfleitner, H., and Sass, O.: Simulation of moisture content in alpine rockwalls during freeze-thaw
746   events: Simulation of Moisture Content in Alpine Rock Walls, Earth Surf. Process. Landforms, 41, 1937–1950,
747   https://doi.org/10.1002/esp.3961, 2016.

748   Roeckner, E., Bäuml, G., Bonaventura, L., Brokopf, R., Esch, M., Giorgetta, M., Hagemann, S., Kirchner, I.,
749   Kornblueh, L., Manzini, E., Rhodin, A., Schlese, U., Schulzweida, U., and Tompkins, A.: The atmospheric general
750   circulation model ECHAM 5. PART I: Model description, Max Planck Institute for Meteorology, Hamburg,
751   Germany, 2003.

752   Sarnthein, M., Gersonde, R., Niebler, S., Pflaumann, U., Spielhagen, R., Thiede, J., Wefer, G., and Weinelt, M.:
753   Overview of Glacial Atlantic Ocean Mapping (GLAMAP 2000): GLAMAP 2000 OVERVIEW,
754   Paleoceanography, 18, n/a-n/a, https://doi.org/10.1029/2002PA000769, 2003.

755   Savi, S., Delunel, R., and Schlunegger, F.: Efficiency of frost-cracking processes through space and time: An
756   example from the eastern Italian Alps, Geomorphology, 232, 248–260,
757   https://doi.org/10.1016/j.geomorph.2015.01.009, 2015.

758   Schaller, M. and Ehlers, T. A.: Comparison of soil production, chemical weathering, and physical erosion rates
759   along a climate and ecological gradient (Chile) to global observations, Earth Surf. Dynam., 10, 131–150,
760   https://doi.org/10.5194/esurf-10-131-2022, 2022.

761   Schmid, M., Ehlers, T. A., Werner, C., Hickler, T., and Fuentes-Espoz, J.-P.: Effect of changing vegetation and
762   precipitation on denudation – Part 2: Predicted landscape response to transient climate and vegetation cover over
763   millennial to million-year timescales, 6, 859–881, https://doi.org/10.5194/esurf-6-859-2018, 2018.

764   Simmons, A. J., Burridge, D. M., Jarraud, M., Girard, C., and Wergen, W.: The ECMWF medium-range prediction
765   models development of the numerical formulations and the impact of increased resolution, Meteorl. Atmos. Phys.,
766   40, 28–60, https://doi.org/10.1007/BF01027467, 1989.

767   Sohl, L., Chandler, M., Schmunk, R., Mankoff, K., Jonas, J., Foley, K., and Dowsett, H.: PRISM3/GISS
768   Topographic Reconstruction, 2009.

769   Sowers, T., Alley, R. B., and Jubenville, J.: Ice Core Records of Atmospheric N2O Covering the Last 106,000
770   Years, Science, 301, 945–948, https://doi.org/10.1126/science.1085293, 2003.

771   Starke, J., Ehlers, T. A., and Schaller, M.: Latitudinal effect of vegetation on erosion rates identified along western
772   South America, Science, 367, 1358–1361, https://doi.org/10.1126/science.aaz0840, 2020.

773   Stepanek, C. and Lohmann, G.: Modelling mid-Pliocene climate with COSMOS, Geosci. Model Dev., 5, 1221–

774   1243, https://doi.org/10.5194/gmd-5-1221-2012, 2012.

775   Turcotte,   D.   and   Schubert,   G.:   Geodynamics,   3rd   ed.,   Cambridge   University   Press,

776   https://doi.org/10.1017/CBO9780511843877, 2014.

777   Valla, P. G., Shuster, D. L., and van der Beek, P. A.: Significant increase in relief of the European Alps during

778   mid-Pleistocene glaciations, Nature Geosci, 4, 688–692, https://doi.org/10.1038/ngeo1242, 2011.

779   Walder, J. S. and Hallet, B.: A theoretical model of the fracture of rock during freezing, GSA Bulletin, 96, 336–

780   346, https://doi.org/10.1130/0016-7606(1985)96<336:ATMOTF>2.0.CO;2, 1985.

781   Wang, X., Schmidt, B., Otto, M., Ehlers, T. A., Mutz, S. G., Botsyun, S., and Scherer, D. . Sensitivity of water

782   balance in the Qaidam Basin to the mid-Pliocene climate. *Journal of Geophysical Research: Atmospheres*, 126,

783   e2020JD033965. https://doi.org/10.1029/2020JD033965, 2021

784   Wei, W. and Lohmann, G.: Simulated Atlantic Multidecadal Oscillation during the Holocene, 25, 6989–7002,

785   https://doi.org/10.1175/JCLI-D-11-00667.1, 2012.

786   Werner, C., Schmid, M., Ehlers, T. A., Fuentes-Espoz, J. P., Steinkamp, J., Forrest, M., Liakka, J., Maldonado,

787   A., and Hickler, T.: Effect of changing vegetation and precipitation on denudation – Part 1: Predicted vegetation

788   composition and cover over the last 21 thousand years along the Coastal Cordillera of Chile, 6, 829–858,

789   https://doi.org/10.5194/esurf-6-829-2018, 2018.

790   Whipple, K. X.: The influence of climate on the tectonic evolution of mountain belts, Nature Geoscience, 2, 730–

791   730, https://doi.org/10.1038/ngeo638, 2009.

792   Wieder, W.: Regridded Harmonized World Soil Database v1.2, https://doi.org/10.3334/ornldaac/1247, 2014.

793